
Article:
Luo, W., Shao, M., Che, X. et al. (4 more authors) (2020) Optimisation of UAVs-SfM data collection in aeolian landform morphodynamics : a case study from the Gonghe Basin, China. Earth Surface Processes and Landforms. ISSN 0197-9337

https://doi.org/10.1002/esp.4965

Luo Wanyin (Orcid ID: 0000-0002-6610-9557)

Hesp Patrick A. (Orcid ID: 0000-0003-4573-2945)

Bryant Robert G. (Orcid ID: 0000-0001-7943-4781)

Optimisation of UAVs-SfM data collection in aeolian landform morphodynamics: A Case study from the Gonghe Basin, China

Wanyin LUO[1]*, Mei SHAO[1], Xuehua CHE[1], Patrick A. HESP[2], Robert G. BRYANT[3]

Changzhen YAN[1] and Zanpin XING[1]

[1] Key Laboratory of Desert and Desertification, Northwest Institute of Eco-Environment and Resources, Chinese Academy of Sciences, Lanzhou, 730000, China.

[2.] Beach and Dune Systems (BeaDS) Laboratory, College of Science and Engineering, Flinders University, Sturt Road, South Australia 5042, Australia.

[3.] Department of Geography, University of Sheffield, Sheffield, S10 2TN, UK

*Corresponding author:

Wanyin LUO, Northwest Institute of Eco-Environment and Resources, Chinese Academy of Sciences, No. 320, West Donggang Road, Lanzhou, Gansu Province 730000, China.

This article has been accepted for publication and undergone full peer review but has not been through the copyediting, typesetting, pagination and proofreading process which may lead to differences between this version and the Version of Record. Please cite this article as doi: 10.1002/esp.4965

E-mail: wyluo@lzb.ac.cn Tel.: +86-(0)931-496-7498

Abstract: UAVs-SfM (Unmanned Aerial Vehicles- Structure from Motion) systems can generate high-resolution 3D topographic models of aeolian landforms. To explore the optimisation of UAVs-SfM for use in aeolian landform morphodynamics, this study tested flight parameters for two contrasting aeolian landform areas (free dune and blowout) to assess the 3D reconstruction accuracy of the UAVs survey compared with field point measurements using differential RTK-GPS (Real-time Kinematic-Global Positioning System). The results reveal the optimum UAVs-SfM flight set-up at the free-dune site was: flying height = 74 m, camera tilt angle = -90°, photo overlap ratio = 85%/70% (heading/sideways). The horizontal/vertical location error was around 0.028~0.055 m and 0.053-0.069 m respectively, and a point cloud density of 463/m3 was found to generate a clear texture using these flying parameters. For the <20m deep blowout the optimum set-up with highest accuracy and the lowest cliff texture distortion was: flying height = 74 m combined camera tilt angle = -90° and -60°, photo overlap ratio = 85%/70% (heading/sideways), and an evenly distributed GCPs (Ground Control Points) density of 42/km2 using these flying parameters. When the depth of the blowouts exceeded 40 m, the optimum flight/survey parameters changed slightly to account for more challenging cliff texture generation: flying height = 80 m (with -90° and -60°combined camera tilt angle), GCPs density = 63/km2 to generate horizontal and vertical location error of 0.024 m and 0.050 m respectively, and point cloud density of 2597.11/m3. The main external factors that affect the successful 3D reconstruction of aeolian landforms using UAVs-SfM are the weather conditions, manipulation errors, and instrument system errors. The UAVs-SfM topographic monitoring results demonstrate that UAVs provide a viable and robust means for aeolian landform morphodynamics monitoring. Importantly, the rapid and high precision 3D reconstruction processes were significantly advanced using the optimal flight parameters reported here.

Keywords: UAVs-SfM; aeolian landforms; precision evaluation; optimum settings; morphodynamic monitoring

1. Introduction

Aeolian landforms are the result of erosion, deposition and transport of sediment by the wind, They exist at a range of scales covering kilometre-scale sand seas and millimetre-scale impact ripples, and encompass a range of morphologies, including dunes and blowouts (Greeley and Nickling, 1998; Hesp and Walker, 2013). They are common morphologies on Earth and also exist on other planets (e.g. Craddock et al., 2012). However, our understanding of the complex interactions between aeolian landforms, windflow and sand transport is often limited by the lack of detailed morphological data at a range of scales (e.g. Conlin et al., 2018). The 3D topography of these landforms is therefore a fundamental component of many studies seeking to either monitor or model these systems (Tarolli, 2014).

To date, accurate 3D topographic surveys often provide the basis for study of the evolution of aeolian (and most) landforms (e.g. Sofia et al., 2016). However, traditional measurement methods are commonly inefficient, with small measurement point densities and compromises in precision position control (Qian et al., 2019). The erosion pin method (e.g. Livingstone, 1989) was originally used to measure topographic change and migration of dunes, but besides time-consuming and laborious, the pins were easily buried by sands causing the monitoring to be difficult to unsustainable (Lancaster, 2009). While theodolites and total station survey instruments have significantly improved field measurement accuracies, they not only need good visual conditions to ensure laser target capture and accuracy but also require frequent movement of the base-station to avoid blind holes (e.g. Young, 2012). The emergence of RTK-GPS provides more convenience for the monitoring of large-scale aeolian landforms under poor visual conditions. However, this measurement method is also time-consuming and laborious, and the low measurement point density still affects the final topographic accuracy. At present, airborne lidar has become a common method to measure terrain changes (Gallay, 2013), but the 3D point cloud generated by this method is relatively sparse and has a large error (Le Mauff et al., 2018). The use of 3D laser scanners improves the density and accuracy of point clouds, but the equipment is expensive to procure, requires careful survey design, good visibility, and is sensitive to surface moisture and large fluctuations in surface roughness (Hodge et al., 2009; Nield et al., 2011; Du et al., 2018; Guisado-Pintado et al., 2019).

Compared with the above methods, UAVs photography through SfM technology added significant advantages, including real-time visualization of data acquisition, and processing for 3D topographic

reconstruction and monitoring in complex landforms (Liao et al., 2018; Zhang et al., 2018; Lucieer et al., 2014 b; James et al., 2019). Furthermore, UAVs-SfM approaches allows the capture of high precision topographic data with lower economic and time costs compared with utilising traditional satellite images and aerial photos (Scarelli et al., 2017). Therefore, UAVs have been widely used in agriculture, forest management (Grenzdörffer et al., 2008), archaeology (Sauerbier et al., 2010), urban planning (Yang, 2018; Zhang, 2018), biology (Li et al., 2019), hydrology (DeBell et al., 2015), earthquake (Valkaniotis et al., 2018), coastal (Guisado-Pintado et al., 2019; Gilham et al., 2019), environmental risk survey monitoring (Caprioli et al., 2016; Balek et al., 2017; Gindraux et al., 2017; Che et al., 2019) and other fields in recent years. However, application of this technique in the field of aeolian geomorphology has been comparatively modest and largely confined to coastal regions (e.g. Taddia et al., 2019), and few of these include available protocols to allow effective utilization of UAVs' to maximise data capture and for use in the geomorphometric analysis of aeolian environments (e.g. Solazzo et al., 2018). Nevertheless, it is clear that large aeolian landforms such as barchans, linear and transverse dunes can be challenging to measure via proximal remote sensing approaches (UAVs, Kites etc), due to steep slopes, presence of shadows, and (in windy conditions) constantly moving sand surfaces (e.g. Solazzo et al., 2018; Duffy et al., 2018). Larger scale topographies such as barchan trains and dune fields, can pose significantly greater issues (Livingstone et al., 2007; Dong and Lu, 2019).

The high resolution and accuracy provided by UAVs images are beyond the reach of satellite derivative products at present, and can be applied in the measurement of some complex landforms (Agüera-Vega et al., 2018). Recent studies utilising UAVs to create 3D morphological models report a range of detailed error estimates. Lucieer et al. (2014a) generated 3D models of a landslide in southeast Tasmania, with a horizontal error of 0.07 m and a vertical error of 0.06 m. Agüera-Vega et al. (2018) discussed the optimal camera angle for using UAVs photography to reconstruct a complex 3D model of a vertical cutting and determined accuracies in x, y and z directions of 0.053 m, 0.07 m and 0.061 m respectively. Chen et al. (2018) monitored coastal erosion with UAVs, and obtained a digital surface model (DSM) with an accuracy of 0.1 m. Guisado-Pintado et al. (2019) compare a ground laser scanner with UAV data and report that UAVs are much more efficient than laser scanners considering the similar accuracy of models generated by the two methods.

From previous studies it has been determined that the x, y and z errors associated with 3D modelling

from a UAVs is generally within 0.1 m (Qian et al., 2019; Chen et al., 2018; Agüera-Vega et al., 2018; Lucieer et al., 2014a), and that appropriate flight conditions and processing parameters are particularly critical for modelling accuracy. Agüera-Vega et al. (2017) and Martínez-Carricondo et al. (2018) discussed the effect of flying height, number of ground control points and their distribution on the accuracy of UAVs photogrammetry for reconstructing orthogonal and digital surface models, but ignored the photograph overlap ratio and camera angle. Moreover, previous studies analyses on the modelling accuracy of a UAVs either only focused on the horizontal and vertical error of the checking points (Agüera-Vega et al., 2017), or only on the density of point clouds (Jaud et al., 2019), with few considering a comprehensive analysis of these two parameters or the modelling texture effect.

At present, the application of UAVs in arid to desert aeolian geomorphological studies (compared to coastal aeolian studies) is not very common for two key reasons: firstly, sand dunes (aeolian landforms) have stronger albedo and subtle image textures. This can lead to data drop-out and black holes in the final models due to the lack of matched feature points and low control point precision in the post processing of photo-mosaics (Seymour et al., 2018). Secondly, the topography in aeolian areas is often complex, and free (unvegetated) dunes may migrate rapidly. For example, the mega-blowouts (giant, wind eroded deflation hollows with dimensions over 100~200 m wide, 1.0~1.5 km long and 40~50 m deep) always have nearly vertical steep side-wall cliffs (Luo et al., 2019a,b), which make it quite difficult to reconstruct the topography using RTK-GPS techniques, and, the detailed topographic changes could not be detected. There are clear gaps to fill given that (a) aeolian processes require specific space/time sampling, and are poorly understood beyond the point scale, and (b) few studies have attempted to optimize/apply SfM accordingly. The key weaknesses in SfM (when compared to LiDAR) are (a) the survey design, and (b) the ground survey element – which is especially important for morphodynamic (repeat) surveys. UAVs photography and three-dimensional (SfM technology provide new opportunities and solutions for the systematic evolution monitoring of large-scale aeolian landforms. Careful design can minimize (a) above, and RTK UAVs can minimize (b) above. Thus, this paper has two principal aims: (i) to develop techniques to optimize SfM to detect morphodynamic changes in aeolian landforms, and (ii) to advance understanding of aeolian landform evolution and dynamics.

In the following sections we assess optimal flight parameters and 3D reconstruction accuracy relevant

to the use of low-cost UAVs-SfM photography for monitoring complex aeolian morphodynamics. The study has been designed to evaluate a range of different UAVs-SfM flight parameters as applied to the investigation of contrasting free dune areas and wind eroded areas (principally mega-blowouts) in the Gonghe basin on the northeast border of Qinghai-Tibet Plateau. A quantitative assessment of the digital orthophoto map (DOM) and digital surface model (DSM) reconstruction accuracy derived from UAVs-SfM (and associated error analysis) were verified using RTK-GPS measured points which were collected simultaneously in the field. In addition, implications of these findings to the application of UAVs-SfM in aeolian geomorphology are both discussed and demonstrated with reference to detailed morphodynamic measurements of free dunes and blowouts in the study area.

2. Data sources and methodology

2.1 Study area

The Qinghai Gonghe basin is located in the northeast of the Qinghai-Tibet plateau which lies between Qinghai Nan Mountain and Bayankala Mountain. Complex topography (mountains, lakes, desert, steppe and river systems) and diverse vegetation types are present reflecting the fact that the region lies in the transitional zone between the westerlies and monsoon climate regimes (Dong et al., 1993; Qiang et al., 2016). The region has a cold arid to semiarid continental climate with an average precipitation of (250~400 mm), mean annual temperature ranging from -0.37~3.7°C and potential evaporation of 1717 mm (Li et al., 2010). Strong north and northwest winds prevail in spring and winter with a maximum wind speed in spring up to 40 m s^{-1}. The region has an average altitude of ~3000 m, glaciers and discontinuous permafrost exists on mountains (Dong et al., 1993; 2017).

There are significant areas of active dunes and wind eroded deflation plains and blowouts in paleo-dunes in the southwest of the Gonghe basin (Fig. 1). Mega-blowouts which have been activated within palaeodunes have seriously destroyed the grassland and threatened the local ecological environmental safety (Luo et al., 2019a, b). Wind erosion has induced more serious sandy grassland desertification in this area, and the local ecological environment has faced increasing damage during the past century. Preliminary dating results reveal that blowouts in this area formed hundreds of years ago, coinciding with the Little Ice Age when winds are thought to have been more intense and a drought is known to have occurred (Luo et al.,

2019b). Rapid 2D extension ratios monitored both by using RTK-GPS and historical remotely sensed track results prove that land degradation is still ongoing (Luo et al., 2019a). But, the detailed 3D erosion/accumulation balance within the deflation basins within the blowouts is still unknown. Further detailed point monitoring using high resolution measurements at the regional scale is required to better understand both the initiation mechanisms and the relationships between blowouts, climate change and human activities.

In this study, in order to explore the modelling accuracy and the best flight parameters of UAVs in different aeolian landforms evolutionary trends, we selected one sand accumulation site (site D, barchan dune site, area 0.9035 km^2, elevation difference 18 m), and two wind eroded landform sites (Site B1, small and middle blowouts sites with an area of 0.3015 km^2, elevation difference 12 m; site B2, mega-blowouts site with an area of 0.3821 km^2, elevation difference 45 m), and compared the areas to determine the application and optimisation of UAVs-SfM to aeolian landform characterization/measurement and identify fine-scale morphodynamic changes to the dunes. Importantly, we also show some initial results stemming from the application of these methods to both quantify and better understand morphyodynamic changes that have occurred at our dune and blowout study locations.

2.2 Materials and Methods:

2.2.1 Equipment

The data source of this study consists of two parts: aerial images and the ground control points system. The UAVs photography was captured utilising a DJI Phantom 4 pro v2 unmanned aerial vehicle (drone) (Fig. 2 C). This UAV weighs 1375 g, has a maximum flying speed of 72 km/h, and a battery life of 20 minutes (The specific parameters are shown in Table S1 in the supplementary file).

2.2.2 Survey Design

The flight planning and photo taking process was completed by DJI GS PRO software. To assess the photography accuracy of 3D modelling produced by PIX 4D and the optimisation of UAVs-SfM to aeolian landform monitoring, we designed seven flying heights (40 m, 50 m, 60 m, 74 m, 80 m , 90 m and 110 m), five photo overlap ratios (heading(the overlap between two adjacent photos in one flight path) /sideways(the overlap between two adjacent photos in two adjacent flight paths): 85%/70%, 80%/70%, 70%/65%, 75%/55% and 65%/60%) and four camera tilt angles (-90°, -60°, -45° and -20°) for comparison (supplementary file, Table S2.) . The density of control points varied from 0 to 38/km^2 at dune site (D) and 0 to 116/km^2 in the wind eroded deflation site (B1 and B2) distributed evenly and randomly. However, due to the battery life limitation of the drone, the flight parameters were adjusted in each area according to the topographic conditions.

2.2.3 Survey Execution

The ground control points (GCPs) markers are made up of 0.5 m × 0.5 m red canvas with 0.05 m wide blue cross stripes. A round hole with a diameter of 0.05 m is located in the middle of the cross stripes to allow the passage of a wooden pole as a control point. A hole with a diameter of 0.01 m is present at the four corners to fix the cloth using an iron pin (Fig. 2 A). To investigate protocols for GCPs layout we installed a high-density GCPs network across our field sites, with 43 ground control/check points at site D, 58 ground control/check points at site B1, and 60 ground control/check points in site B2. The coordinate system information for ground control/ check points were measured using RTK-GPS (TOPCON, GR-3) with 10-20 mm horizontal and 20-30 mm vertical accuracy (Fig. 2 B).

2.2.4 Processing Software

The images taken form the UAVs were processed with SfM and multi-view stereo approach in PIX 4D mapper software (4.3.31). There are three major steps in the software to process the images from UAVs, including initial processing, point cloud and mesh, DSM and DOM. Five specific steps were required to generate the DSM and DOM (Fig. 3).

2.2.5 Errors and Uncertainty

Modelling accuracy assessment was mainly carried out using three fundamental aspects of the output data: (i) location accuracy, (ii) point cloud effects, and (iii) model texture. The location accuracy of Otho-image and DSM generated by UAVs modelling was tested using field measured check points and lines. The GCPs and CPs coordinates measured by RTK-GPS in the field were manually input into the PIX 4D software for each of the raw image mosaics to calculate the points location errors (horizontal error, d_{Hi} and vertical error d_{Vi}) and root mean square errors (RMSE) for the whole flying plan using the following equation:

$$RMSE_H = \sqrt{\frac{1}{\mathrm{n}}\sum_{i=1}^{\mathrm{n}} d_{Hi}^2} \quad (1)$$

$$RMSE_V = \sqrt{\frac{1}{\mathrm{n}}\sum_{i=1}^{\mathrm{n}} d_{Vi}^2} \quad (2)$$

$$d_{Hi} = \sqrt{(x_i - x_i')^2 + (y_i - y_i')^2} \quad (3)$$

$$d_{Vi} = \sqrt{(z_i - z_i')^2} \quad (4)$$

where, $RMSE_H$ is the horizontal root mean square error of all ground control/ check points, while $RMSE_V$ is the vertical root mean square error of all ground control/ check points. x_i, y_i, and z_i are the real horizontal and vertical coordinates of the GCPs measured by RTK-GPS in the field, x_i', y_i', and z_i' are the calculated horizontal and vertical coordinates of point *i* generated by the 3D UAV reconstructed models through SfM photogrammetry, d_{Hi} and d_{Vi} are the horizontal and vertical location errors of point *i* respectively.

The 3D point clouds density and the texture clarity of the sand ripples on the dune (D) and the side wall cliffs of the blowout (B1) from the DOM were also considered in detail to assess the UAVs' modelling results. Furthermore, in order to further verify the reliability of the 3D modelling of low-cost UAVs, the elevation values of the dune ridge (D) and the blowout margin (B1) were extracted through the reconstructed DSM models as the check lines (made up of multiple points) using ArcGIS 10.0 software, we fitted the

elevation values of the same points in the check lines extracted from RTK-GPS and UAVs. There are three steps utilised to obtain the elevation of the check lines in ArcGIS 10.0. Firstly, we digitally vectorized the edges of site D and site B1; then, we extracted the elevation of DSM and RTK-GPS based on the vectorized files using the tool "extract values to points"; finally, we export the attribute value of the extracted points.

2.2.6 Application of optimal SfM configuration at the field sites

The final stage of our analyses involved the use of optimised UAV-SfM survey data to both quantify morphdynamic changes that have occurred at our study sites, and to demonstrate the importance of SfM configuration to the study of dynamic erosional and depositional aeolian landforms. At site B2 (a mega-blowout) our assessment was based on UAVs-SfM topographic monitoring results for data collected over multiple years (2017, 2018 and 2019). At site D1 (a moderate sized barchan dune), our assessment involved the use of UAV-SfM data to track the short-term (from March to June 2019) topographic changes. For each of these case studies, ground control data were used to carefully co-register DOM and DSM data taken at different times.

3. Results and Discussion

The key parameters that affect the 3D reconstruction accuracy of a UAVs are principally the flight height (cf. pixel size), photo overlap, camera tilt angle, density of GCPs and their distribution. Therefore, this study considered the locationaccuracy, point cloud density and texture effect of the final UAVs photogrammetry model to assess the 3D reconstructive accuracy.

3.1 Controls on Error and Uncertainty in SfM Outputs

3.1.1 SfM location Accuracy

The quality of photogrammetric results can not be evaluated by simply stating the error observed at control measures. Any assessment of data quality must involve comparison with independent check point coordinates, surfaces or length measurements, or by using a split test (James et al., 2019). In order to further evaluate the accuracy of UAVs 3D modelling, we compared the elevation values of ground check points and check lines (some characteristic lines which were selected to assess the accuracy of 3D modelling) extracted from the digital surface model (DSM) with their real value measured by RTK-GPS. In Guisado-Pintado's

(2019) study, a fit of linear regression for TLS and SfM-UAV elevations versus the GPS was conducted, and they determined a R^2 ranging from 0.891 to 0.999. In this study, one task was selected in each of the two study areas for verification, and the verification results are shown in Fig. 4 and 5. In the morphological evolution monitoring of aeolian landforms, it is common to pay more attention to the morphological changes of some characteristic parts or landform units. So, we compared the characteristic lines elevation difference extracted from both the UAVs-SfM and RTK-GPS reconstructed DSM model in the dune (site D) and blowout (site B1) areas to assess their 3D modelling accuracy. Results from the linear regression plots (Fig. 4 and 5) showed that the correlation between the UAVs-SfM extracted elevations fitted well with the RTK-GPS values collected by hand-held pole. The accuracy of the stoss slope and dune ridge was slightly higher than that of the leeward bottom (Fig. 4). This may be because the leeward slope of the dune was steeper causing higher albedo than the stoss slope, and hence, produced a lack of matching points during 3D reconstruction. In the wind erosion site (site B1 in Fig. 5), the accuracy of the side wall slopes was less than the bottom part, which may also be because of complex topography within the deflation basin. The side wall was closest to the camera under the same flight height, the scope of each photo was small compared to the bottom area, thus, fewer feature points can be matched during the post-processing. Furthermore, the surface of the blowout side wall was mostly covered by fine sand which has the same albedo as the dune stoss slope compared to the gravel and grass covered base of the deflation basin.

There was a high correlation between the elevation measured in the field and the elevation of the DSM obtained by UAVs modelling, which shows that the method of 3D terrain reconstruction with UAVs is reliable and its modelling accuracy is much higher than RTK-GPS method.

Flight height not only determines the resolution of modelling (i.e. base pixel size), but also affects the location accuracy, and the ability to detect landform components (and hence their change over time); this is especially important for aeolian landforms. In Hugenholtz's (2015) research, they yield a value of $RMSE_{xy}$ equal to 0.039 m when they carried a test with a flight altitude of 118 m and 11 GCPs compared a $RMSE_{xy}$ equal to 0.106 m with a flight altitude of 118 m and 10 GCPs. Their result illustrated that the flight altitude and GCPs would influence the location accuracy. So, we conducted a set of tests to explore the effect of flight altitude.

The optimal flight height of the two landforms studied here varies notably, and this is due to the obvious difference in topographic relief, surface condition and scale. Due to the large area of dune site D (area is 0.9035 km^2), we also note some key logistic constraints, as data volume (which is a function of survey density) is limited by available UAVs battery life and can lead to a compromise in flight requirements, as recharging in the field (even using a generator) is slow. Therefore, in this instance, only 74 m, 90 m and 110 m flights were conducted, and at dune site D1, we conducted the 40 m and 50 m flights planning only as a supplement. According to the experimental results (Table 1), the location accuracy shows an overall rising trend with an increase of the flight height in barchan dune area. The horizontal location error decreases, while the vertical location error increases with an increase in flight height in site B1, and the accuracy of the 3D modelling tends to improve. For the mega-blowout B2, when the flight height increased from 60 m (heading/sideways overlap 85%/70%) to 80 m (heading/sideways overlap 80%/70%), the horizontal location accuracy was increased, but the vertical location accuracy decreased.

As shown in Table 2, the GCPs location accuracy increased dramatically with a decrease of the overlap ratio in both the dune and blowout sites. However, the check points location accuracy shows no obvious variation with the overlap ratio change. In the barchan dune area, the best positioning accuracy appeared where the overlap was 85%/70%. In blowout site B1, the CPs location accuracy of the 85%/70% overlap was better than the 75%/55% overlap, but the difference was just a few millimeters. In Agüera-Vega's (2018) research, he found that the best location accuracy appeared when they combined the images taken with the camera tilted at 45° and oriented horizontally. Also, as revealed in Table 3, both the GCPs and CPs location accuracy decreases as the camera angle increases from -90° to -20° in the dune area, especially for the CPs which decreased more than two times. When the camera angle changes from -90° to -45° in blowout B1, the horizontal accuracy and the vertical accuracy remains stable. When it changes from -90° to -60°, the horizontal accuracy remains unchanged and the vertical accuracy is decreased by 5 mm, but with a slight variation in the blowout area. Therefore, the location accuracy is significantly affected by the camera angle at the dune site, but has no significant difference in the blowout sites.

The density of GCPs would influence the location accuracy of the CPs. In Agüera-Vega's (2017) study, the location accuracy of $RMSE_z$ experiences a large drop when the number of the GCPs changed from 4 to

5, which is similar to our result in B1. Both the horizontal and vertical location accuracy of check points decreased with the decrease of the density of control points in the dune and blowout sites (Table 4). In the D area, when the density of control points is 29/km^2, the location accuracy of the check points is the highest. When the number of control points is 0, the horizontal error of the checkpoint is about 0.7 m and the vertical error is about 27 m. In the B1 area, when the number of control points is greater or equal to 42/km^2, the accuracy of the checkpoint changes little with a decrease in the number of control points. When the number of control points drops to 25/km^2, the vertical accuracy also drops significantly. When the density of control points is 0, the horizontal accuracy of the checkpoint drops to 0.67 m. The check points horizontal and vertical location error decreased two to four times when the control point was distributed evenly at the dune site. The check points horizontal location error decreased gently, while the vertical location error decreased dramatically from 60 mm to 46 mm in B1 (Fig. 6, Table 5).

3.1.2 Point cloud density

Fig. 7 shows the variation in trends of the point cloud density of the reconstructed models with different parameters. Note that we have also found that different options in the PIX 4D (optimal (default), high (slow), low (fast)) can impact the point cloud density, so we set the "optical (default)" option in the photo processing in PIX 4D to ensure that the point cloud density was not artificially affected. The point cloud density decreases with an increase of the flight height both at site D and B1 (Fig. 7 A). In the dune area, when the flight height increases from 40 m to 110 m, the density of the point cloud decreased by 95%. The density of the point cloud decreases by 84% with the flight height increasing from 40 m to 74 m in the blowout area (sites B1 and B2). The point cloud density decreased from 463/m^3 to 406/m^3 with the overlap ratio decreasing from 85%/70% (heading/sideway) to 65%/60% (heading/sideway) in the dune area. However, the point cloud density increased from 3086/m^3 to 3341/m^3 when the overlap ratio decreased from 85%/70% (heading/sideway) to 75%/55% (heading/sideway) at the blowout site. Therefore, the photo overlap ratio has little influence on the point cloud density. Similarly, the point cloud density had no significant change with the change in the density and distribution mode of GCPs in all sites (Fig. 7 C and D). However, the camera tilt angle has a great influence on the point cloud density. The point cloud density increases rapidly with an increase of camera tilt angle no matter which site is considered (D or site B1). In general, as expected, flight height and camera tilt angle can be used to significantly affect the point cloud density of the final 3D model.

Where landform complexity and rate of change are significant, it is clear that a lower flight height and higher camera angle can be used to generate a higher point cloud density, and generate a higher resolution 3D model.

3.1.3 Modelling texture effects

The key factors that affected the 3D modelling texture which is similar to the 3D anomalies mentioned by Seymour (2018) were the relative impacts of image clarity/contrast and distortion. The texture of the final model in each case can be inferred by tracking the relative clarity of sand ripples on the dune surface and the side wall cliff at the edge of the blowout (Fig. 8). It was clear that as the flight height increased (and resolution in pix/cm decreased), the sand ripples and the cliff texture (red box area) were becoming more and more obscure for both the dune site and the blowout site, which means that the clarity of the model declined due to the decrease of the surface model resolution.

As was shown in Fig. 9, many black holes and bar shadows appeared in the UAV generated orthomosaic image when the photo overlap ratio was 75%/55% (heading/sideway), while these disappeared when the overlap ratio was 85%/70%(heading/sideway) in the blowout site. Meanwhile, the texture of sand ripples did not change greatly with a decrease of overlap ratio at the dune site.

At the same time, we compared the texture effect of 3D modelling with different camera angles (Fig. 10). A net effect of increasing of the camera view angle was that the flight area became larger and the edges of the survey became uneven (especially at the dune site). However, we can also see that the texture clarity of sand ripples on the dune surface also decreased as the camera angle changed between -90° and -20°, with features having especially low contrast (leading to poor model texture and image distortion) when the angle was -20°. At the blowout site (B1), an increase in the camera view angle caused the appearance of bar shadows in the orthomosaic image, which was similar to Jaud et al's (2019) results in beach cliff monitoring using a UAV. However, considering the improved texture of the blowout cliff in these data, the multi-oblique view angle flight data were significantly better at capturing landform characteristics than simple vertical camera capture (Fig. 11).

3.1.4 Comprehensive accuracy assessment of the reconstruction modelling from UAVs-SfM

As may be seen from the above results, due to the high ground albedo and sparse vegetation, the flight height, overlap ratio, camera tilt angle and the number and distribution of GCPs have certain influences on the position accuracy, point cloud density and texture effect of both the depositional and erosional sandy landforms, but the degree of influence of each parameter varies.

As may be expected, the flight height requirements for the monitoring target and research areas were different and, consequently, these changes were likely to impact on modelling accuracy (Laporte-Fauret et al., 2019; Scarelli et al., 2016; Qian et al., 2019). In this study, the minimum RMSE appeared at a flight height of 110 m ($RMSE_{x,y}$ =0.057 m, $RMSE_{z}$ =0.023 m), which was slightly larger than the results of Scarelli et al. (2016) and Qian et al. (2019), but better than the accuracy of Laporte-Fauret et al. (2019). From our research, the overall positional accuracy was strongly correlated with the flight height (and pixel size). This is most likely the result of that fact that as flight height/pixel size is increased the field of view of each photo becomes larger. As a consequence, the number of matching points between neighbouring photos is increased during post-processing, resulting in lower apparent distortion of each photo and an increase in the position accuracy. However, given that the point cloud density decreased as flying height increased, the trade-off in this case is a reduction in texture clarity. Therefore, in surveying landforms at this scale using UAVs-SfM, a compromise must be reached between geomorphometric clarity (essential for characterising the landform) and base-line geometric accuracy (essential for the detection of landform change). In this instance the most appropriate flight height for aeolian landform monitoring was found to be 74 m; which is broadly comparable (85 m) to that used by Laporte-Fauret et al. (2019).

For consumer UAVs, high photograph overlap results in the need to factor-in increased battery power use, survey time, and data volume, which in turn, increases time and resource use during data post-processing. In Laporte-Fauret et al's (2019) coastal dune experiment, the photo overlap ratio was 75%/55% (heading/sideways, flight height was 85 m), and the vertical reconstruction error was 0.05m. In this study, low vegetation cover made image matching significantly harder in the dune area, where the overlap ratio changed and the positional accuracy fluctuated (Table 2). At site D, there was no significant difference in the texture of orthoimages as a result of changes to the overlap ratio. Although point cloud density change was found to be minimal, positional accuracy was observed to be highest when the overlap was 85% / 70%

(heading/sideways). In contrast, at sites B1 and B2 the positional accuracy and the point cloud density were both slightly improved with a decrease of the overlap ratio. However, there were other compromises, as many holes and bar shadows were apparent in the orthoimage when the overlap ratio decreased to 75% / 55% (heading/sideway), which seriously affected quality of the output DSM model. Therefore, we suggest 85% / 70% (heading/sideway) to be the optimal overlap ratio whether in sand accumulation sites (site D) or wind erosional sites (site B1 and B2).

Our results concur with Jaud et al. (2019), who also found that the modelling effect of oblique photography outperformed vertical photography. However, in addition, our results show that the increase in camera view angle can also lead to a reduction in location accuracy in dune areas. The reasons for this may be as follows: Firstly, as noted above, the distortion of the ground objects increased with an increase of the camera tilt angle, leading to a decrease in the positional accuracy. Secondly, due to the tilt of the camera, the area of the photographed ground objects increased, resulting in a decrease of the point cloud density, and some ground objects were blurred. Therefore, the optimal camera angle is -90° (nadir) in the dune area. For the wind-eroded area (site B1 and B2), an increase of camera angle has little effect on the location accuracy, but has a great influence on the cliff texture effect of the blowout side wall. Especially for the mega-blowout (B2) with a large elevation difference, the steep cliff of the model built using a vertical camera angle was distorted and unclear, while the modelling effect using the oblique camera angle was better (Fig. 11) than vertical angle, which is consistent with Jaud et al's (2019) conclusion. Therefore, although using a vertical angle of the camera can meet the location accuracy requirements of orthophoto images in the wind- eroded area, the combined -60° and -90° camera angle has more advantages in terms of texture effect.

GCPs density also plays a decisive role in the 3D reconstruction accuracy, as the GCPs' density decreased, the position accuracy will decrease obviously due to the fact that reconstruction precision is calculated with the adjustment of GCPs (Fig. 12). Accordingly, Gindraux et al (2017) proposed a function of the GCPs density and location accuracy:

$$\sigma = a \times \exp(-b \times \rho_{GCPs}) + c \quad (5)$$

where σ represented the horizontal and vertical errors of GCPs, *a, b, c* were coefficients derived from the curve fitting, and ρ_{GCPs} represented the density of GCPs.

We used function (5) to examine the relation between position accuracy and GCPs' density in this research. Our results reveal that the positional accuracy of 3D reconstruction increased obviously with an increase of the GCPs' density, but slowed down to a balanced state after reaching a certain density (Fig. 12 A), which agrees well with the result of Gindraux (2017). The vertical RMSE value (named value σ in function 5) was quite large which was caused by the high UAVs positional error without GCPs georeferenced photogrammetry. Considering that GCPs' number has no significant influence on point cloud density and texture effect, the optimal control point density for the sand accumulation landforms was 29/km^2. The result for the wind eroded landform (site B1) (Fig. 12B) was quite different from site D, but this does not affect the trend of accuracy which decreased with an increase of the control point density. In site B1, the control point density of 42 / km^2 is the best, which was consistent with the control point density of Caprioli et al (2016) using a UAVs for 3D modelling in a coastal area.

To ensure the accuracy of local features, GCPs must be evenly distributed. Martínez-Carricondo et al (2018) pointed out in their study that placed the GCPs at the edge of the area under investigation was conducive to reduce the error of the 3D reconstruction, and a stratified arrangement was also needed. However, in this study, we found that an uneven distribution of GCPs will sharply reduce the positional accuracy, and it is the best scheme to place GCPs at an interval of 200 m at the dune site, 150 m in the shallow depression area (site B1, a small to medium sized blowout), and 100 m in the deep depression area (site B2, a mega-blowout). This density setting of GCPs was slightly different from that set in Laporte-Fauret et al (2019), which was caused by the different density levels of the two experimental settings.

3.1.5 Overall assessment of Error sources

The main sources which can produce errors to the UAVs-SfM modelling were weather conditions, human factors and the operational system. The weather factors that affect the UAVs 3D modelling mainly include sun light intensity and wind conditions. For aeolian landforms, too strong light intensity will directly enhance the ground surface albedo (the albedo information is added in the supplementary file, Table S3), and cause the photo brightness to be too high, and then this will affect the extraction of feature points during the auto-post-processing on a computer, and thus, ultimately affect the quality of the reconstructed model. Excessive wind, however, will affect the stability of the UAVs, not only increasing the risk of losing contact

with the UAVs, but also reducing the precision of its location and the sharpness of the photos taken, which in turn leads to a decrease of the matching points number and point cloud density, and finally increases the accuracy error of modelling. Human factors that affect the 3D reconstruction model quality of UAVs include two parts: one is from GCPs' coordinate location during the manual input process; and the other is from the field ground hand-held pole survey. Human-made errors were inevitable during the georeferencing processes using the GCP's coordinate information generated by RTK-GPS. To minimize this kind of error, the roving station pole is positioned vertically on the top of the GCPs for 1min until it is stable before collecting the data. Meanwhile, we always had a GCPs coordinate in at least 4 photos to adjust the input error during the georeferencing process in PIX 4D mapper, which will greatly reduce the human error; In addition, magnifying the image to pixel level and then inserting the point can control the artificial error within 10 mm. The system errors though out the UAVs-SfM modelling mainly come from two aspects: UAV's aerial-positioning error, and RTK-GPS measuring error (±0.005~0.03 m). The aerial-positioning error of a low-cost consumer UAVs (DJI Phantom 4 pro) is 1-2 m under good weather conditions, and would be higher under bad weather conditions. The GCPs measuring error from the GPS system itself was inevitable (horizontal error was 10-20mm, vertical error was 20-30 mm), which leads to a 10-20 mm error in the coordinates measurement of GCPs during post-processing.

3.2. SfM contribution to understanding aeolian landforms at the field sites

3.2.1 Medium-term topographic changes of the mega-blowout

In order to further evaluate the advantages and application prospects of the consumer UAVs in aeolian geomorphological research, the two dimensional horizontal expanding ratio and the three dimensional erosion/accumulation differences within the mega-blowout in site B2 based on the UAVs-SfM topography monitoring results in 2017, 2018 and 2019 were calculated to monitor its dynamic evolution processes (Fig. 13). The optimal flight parameters were conducted and ground control points were also used to guarantee the modelling accuracy of the DOM and DSM in the time series flights. The mega-blowout at site B2 was under an expansion state in these three years while the extension ratios varied in different parts from the UAVs monitoring results. The 2D horizontal expansion rate of the headwall was up to 1.35 m per year, much faster than the side wall (0.3 m a^{-1} in the northeast and 0.4 m a^{-1}in southwest respectively). Meanwhile, the

horizontal expansion rate of this mega-blowout from 2018 to 2019 was significantly higher than that from 2017 to 2018, showing a different extent of spatial extension.

The DSM difference between 2017 and 2019 indicated that, due to the marginal cliff collapse, the maximum erosion depth of the headwall was up to 2 m, and the northeast sidewall of the mega-blowout was eroded around 0~1.99 m with an average erosion depth 1~1.5 m. However, the slump slope of the headwall and the sidewall showed accumulation trends, and the mean accumulation depth was 0~0.5 m, which was mainly due to the settlement of the collapsed soil blocks from the cliff. This patchy erosion and deposition pattern on the northwest slope of the blowout was caused by the coupling of the secondary air flow entrainment and the continued collapsing and settlement from the top surface soil blocks (Hesp et al., 2002; 2016). There was also a staggered distribution of patchy accumulation and erosion at the bottom of the deflation basin. Even though the blowout was dominated by erosion under the prevailing wind, a large number of coarse particles are also deposited on the deflation base or floor under the action of gravity at the same time. The downwind part within the blowout was dominated by accumulation, with the maximum deposition depth of 1 m and an average deposition depth of 0~0.5 m on the depositional lobe.

3.2.2 Short-term topographic changes on a small barchan dune

Fig. 14 shows the short-term (from March to June 2019) topographic changes of a monitored moderate sized barchan dune at site D1. In general, the barchan dune moved rapidly southeast during the monitoring period, with different parts of the barchan dune migrating at different rates. The windward slope, right-wing slope and leeward slope moved relatively faster with a maximum migration rate of 2.56 m M^{-1}(meter per month), 2.93 m M^{-1} and 1.08 m M^{-1} respectively during the three months, while the left-horn movement of the dune moved slightly slower with a maximum migration rate of only 0.23 m M^{-1}. On a 3D scale, the sand erosion and deposition also varied spatially. The windward slope was mainly eroded to a depth varying from 0~1.0 m, while the leeward slope of the dune was mainly depositional with an average deposition depth around 1.0~2.0 m, which was caused directly by the forward movement of the ridge line. Due to the measurement errors in the field and indoor post-possessing, the calculation result has some errors. But the total survey time required for each site shows that surveys using an UAVs are faster to implement compared to RTK-GPS surveys, and furthermore, the higher quality of the surface models generated using UAVs-SfM

has more advantages especially in complex terrain in wind deflation and blowout areas.

4. Conclusions

Through a series of comparative experiments, this study analysed and discussed the optimal flight parameters and their influencing factors when the UAVs-SfM is used to model a large area (~1 km^2) over aeolian landforms. The results show that the optimal flight height is ~74 m and, the overlap is 85% / 70% (heading/sideway) with the camera angle set at - 90 ° over the sand dune area. The vertical and horizontal RMSE (root mean square error) were around 0.028~0.055 m and 0.053-0.069 m respectively under these flight survey parameters. To achieve this, the density of GCPs is 29 / km^2, and evenly distributed at an interval of 200 m for DSMs' georeferencing. For the wind eroded blowout/deflation areas, the optimal flight height is 74 m and, the overlap is 85% / 70% (heading/sideway) with the camera angle combined with - 90 ° and - 60 ° angles if the blowout depth is less than 20 m. The density of GCPs is 42 / km^2, and evenly distributed at an interval of 150 m to achieve this precision. However, if the blowout depth is greater than 40m, the suggested suitable flight parameters are as follows: a flight height of 80m, overlap of 80% / 70%(heading/sideway), camera angle of - 90 ° and - 60 °, and density of GCPs is 63 / km^2 evenly distributed at an interval of 100 m. In order to reduce the position error and improve the model accuracy, a sunny and windless day should be selected as far as possible when carrying out a UAVs survey.

At present, there are still some problems still unsolved in UAVs-SfM 3D modelling: (1) Some flight parameters are not clear. Due to the limitations of the field flight conditions, the optimal flight parameters for aeolian landforms (large sand dunes and mega blowouts) with an elevation difference greater than 40m are still not clear. (2) How to solve the texture distortion of the model? Although increasing flight side overlap can reduce the degree of distortion, distortion cannot be completely eliminated, so how to completely eliminate the distortion is still a large problem that needs to be solved. (3) Black hole in the orthoradial image. According to our research results, the black hole of the model is a universal problem no matter whether one is examining sand accumulation or wind eroded landforms and the cause and solution of the black holes are unknown. A conjecture is that they may caused by the strong albedo of the sand, but this has still to be verified and requires further exploration. (4) Quantitative analysis of modelling accuracy influenced by the local terrain and environmental factors. At present, only qualitative analysis of the impact of local terrain

has been carried out, but no further analysis has been conducted on factors such as the impact of terrain slope and vegetation coverage on modelling accuracy.

Preliminary minor results revealed that compared with the previous artificial single-point measurements by an RTK-GPS (Luo et al., 2019a), the accuracy by using UAV modelling improved at least 50 times (GPS measurement step is 0.05~0.1 m along the edge, but 5~10 m in the deflation basin, while UAV modelling resolution is 0.01~0.03 m in the whole deflation area). By virtue of its high accuracy, and clear and visible texture effect of the orthoimage, we can dynamically compare the high resolution topographic changes of the blowout, calculate the mass balance within the deflation basin to analyse the dust emission quantity and, accurately detect the migration and 3-D topographic changes of sand dunes from short-term event scales to long-term yearly scales. More importantly, because of their portability, low cost, and rapid survey time and ease of deployment capabilities, UAVs-SfM have clear advantages in data acquisition over other topographic survey techniques. We believe that UAVs-SfM will have a very promising application prospect in aeolian landforms morphodynamical monitoring, particularly over the complex mega deflation/blowout landforms in the future.

Acknowledgments:

This study was supported by the National Natural Science Foundation of China (41771015) and the PIFI scholarship (2017VCA0006) awarded to Patrick Hesp. Many thanks to all field companions without whom data collection would not have been possible. Permission to conduct the research and additional logistical support was provided by Huoxian Yang and his family. Many thanks to Professor ChangzhenYan and Miss Zanpin Xing for the drone use and technical support. Many thanks to the State Key Laboratory of Cryospheric Science for the permission to use the PIX 4D software process the photos. Wanyin Luo and Robert Bryant sincerely thank the Thesiger Oman International Fellowship from the Royal Geographical Society (with IBG) for the support of internal travel expenses. Many thanks for the constructive comments and suggestions from the three reviewers' and the editors, which have significantly helped to improve the manuscript.

Data statement: The data sets used and/or analysed during the current study are available from the corresponding author on reasonable request.

Conflict of interest statement: No conflict of interest in this manuscript

References:

1. Agüera-Vega F, Carvajal-Ramírez F, Martínez-Carricondo P. 2017. Assessment of photogrammetric mapping accuracy based on variation ground control points number using unmanned aerial vehicle. Measurement 98: 221-227.

2. Agüera-Vega F, Carvajal-Ramírez F, Martínez-Carricondo P, López JSH, Mesas-Carrascosa FJ, García-Ferrer A, Pérez-Porras FJ. 2018. Reconstruction of extreme topography from UAV structure from motion photogrammetry. Measurement 121: 127-138.

3. Balek J, Blahůt J. 2017. A critical evaluation of the use of an inexpensive camera mounted on a recreational unmanned aerial vehicle as a tool for landslide research. Landslides 14(3): 1217-1224.

4. Caprioli M, Trizzino R, Mazzone F, Scarano M. 2016. Experiences of UAV surveys applied to environmental risk management. The International Archives of Photogrammetry. Remote Sensing and Spatial Information Sciences 41: 797-801.

5. Chen BQ, Yang YM, Wen HT, Ruan HL, Zhou ZM, Luo K, Zhong FH. 2018. High-resolution monitoring of beach topography and its change using unmanned aerial vehicle imagery. Ocean and Coastal Management 160: 103-116.

6. Che YJ, Wang SJ, Liu J. 2019. Application of Unmanned Aerial (UAV) in the glacier region with complex terrain: a case study in Baishui River Glacier No.1 located in the Yulong Snow Mountains. Journal of Glaciology and Geocryology 41(1): 1-9. (in Chinese with English Abstract)

7. Conlin M, Cohn N, Ruggiero P. 2018. A Quantitative Comparison of Low-Cost Structure from Motion (SfM) Data Collection Platforms on Beaches and Dunes. Journal of Coastal Research 34, 1341–1357. doi:10.2112/JCOASTRES-D-17-00160.1.

8. Craddock RA. 2012. Aeolian processes on the terrestrial planets: Recent observations and future focus. Progress in Physical Geography, 36(1), pp.110-124.

9. Dong ZB, Hu GY, Qian GQ, Lu JF, Zhang ZC, Luo WY, Lü P, 2017. High-altitude aeolian research on the Tibetan Platteau. Reviews of Geophysics 55 :864-901.

10. Dong ZB, Lü P. 2019. Aeolian geomorphology in the era of deep space exploration. Advances in Earth Science 34(10): 1001-1014. (in Chinese with English Abstract)

11. Dong GR, Gao SY, Jin J. 1993. Land Desertification and Control Ways in Gonghe Basin of Qinghai Province. Beijing. Science Press. (in Chinese with English Abstract)

12. Du C, Zhao J, Ren XY, Zhang L, Zhuang YH. 2018. The review of TLS technology in environmental and geological disaster monitoring. Science of Surveying and Mapping 43(06): 65-71. (in Chinese with English Abstract)

13. DeBell L, Anderson K, Brazier RE, King N, Jones L. 2015. Water resource management at catchment scales using lightweight UAVs: Current capabilities and future perspectives. Journal of Unmanned Vehicle Systems 4(1): 7-30.

14. Duffy J, Shutler, J, Witt M, DeBell L. Anderson K. 2018. Tracking fine-scale structural changes in coastal dune morphology using kite aerial photography and uncertainty-assessed structure-from-motion photogrammetry. Remote Sensing 10(9): 1494.1-21.

15. Gallay M. 2013. Direct acquisition of data: airborne laser scanning. Geomorphological techniques 2(1.4) : 1-17.

16. Gindraux S, Boesch R, Farinotti D. 2017. Accuracy assessment of digital surface models from unmanned aerial vehicles' imagery on glaciers. Remote Sensing 9(2): 186.1-15.

17. Greeley R, Nickling WG. 1998. Aeolian landforms: laboratory simulations and field studies. In *Aeolian Geomorphology: Binghamton Geomorphology Symposium 17* (Vol. 2). Routledge.

18. Grenzdörffer GJ, Engel A, Teichert B. 2008. The photogrammetric potential of low-cost UAVs in forestry and agriculture. The International Archives of the Photogrammetry. Remote Sensing and Spatial Information Sciences 31(B3): 1207-1214.

19. Guisado-Pintado E, Jackson DW, Rogers D. 2019. 3D mapping efficacy of a drone and terrestrial laser scanner over a temperate beach-dune zone. Geomorphology 328: 157-172.

20. Gilham J, Barlow J, Moore R. 2019. Detection and analysis of mass wasting events in chalk sea cliffs using UAV photogrammetry. Engineering geology 250: 101-112.

21. Hesp P. 2002. Foredunes and blowouts: initiation, geomorphology and dynamics. Geomorphology 48(1-3): 245-268.

22. Hesp PA, Smyth TA, Walker IJ, Gares PA, Wasklewisz T. 2016. Flow within a trough blowout at Cape Cod. Journal of Coastal Research 75(sp1): 288-293.

23. Hesp, PA, Walker IJ. 2013. Aeolian environments: coastal dunes. In: Shroder, J. (Editor in Chief), Lancaster, N., Sherman, D.J., Baas, A.C.W. (Eds.), Treatise on Geomorphology, vol. 11, Aeolian Geomorphology. Academic Press, San Diego, CA, pp. 109-133.

24. Hodge R, Brasington J, Richards KS. 2009. Analysing laser-scanned digital terrain models of gravel bed surfaces: linking morphology to sediment transport processes and hydraulics Sedimentology 56(7): 2024–2043.

25. Hogenholtz CH, Walker J, Brown O, Myshak S. 2015. Earthwork volumetrics with an unmanned aerial vehicle and softcopy photogrammetry. Journal of Surveying Engineering 141(1): 06014003.1-06014003.5.

26. Jaud M, Letortu P, Théry C, Grandjean P, Costa S, Maquaire O, Davidson R, Le Dantec N. 2019. UAV survey of a coastal cliff face–Selection of the best imaging angle. Measurement 139: 10-20.

27. James MR, Chandler JH, Eltner A, Fraser C, Miller PE, Mills JP, Noble T, Robson S, Lane SN. 2019. Guidelines on the use of structure-from-motion photogrammetry in geomorphic research. Earth Surf. Process Landforms 44: 2081–2084.

28. Lancaster N, 2009. Aeolian features and processes, in Young, R., and Norby, L., Geological Monitoring: Boulder, Colorado, Geological Society of America p. 1-25, doi: 10.1130/2009.monitoring(01)

29. Laporte-Fauret Q, Marieu V, Castelle B, Michalet R, Bujan S, Rosebery D. 2019. Low-Cost UAV for high-resolution and large-scale coastal dune change monitoring using photogrammetry. Journal of Marine Science and Engineering 7(3): 63.1-16.

30. Livingstone I. 1989. Monitoring surface change on a Namib linear dune. Earth Surface Processes and

Landforms 14(4): 317-332.

31. Livingstone I, Wiggs GFS, Weaver CM. 2007. Geomorphology of desert sand dunes:A review of recent progress. Earth-Science Reviews 80(3-4):239-257.

32. Luo WY, Wang ZY, Shao M, Lu JF, Qian GQ, Dong ZB, Bateman MD. 2019a. Historical evolution and controls on mega-blowouts in northeastern Qinghai-Tibetan Plateau, China. Geomorphology 329: 17-31.

33. Luo WY, Wang ZY, Lu JF, Yang LH, Qian GQ., Dong ZB, Bateman MD. 2019b. Mega-blowouts in Qinghai–Tibet Plateau: Morphology, distribution and initiation. Earth Surface Processes and Landforms 44(2): 449-458.

34. Lucieer A, de Jong SM, Turner D. 2014. Mapping landslide displacements using Structure from Motion (SfM) and image correlation of multi-temporal UAV photography. Progress in Physical Geography 38(1): 97-116.

35. Lucieer A, Turner D, King DH, Robinson SA. 2014. Using an Unmanned Aerial Vehicle (UAV) to capture micro-topography of Antarctic moss beds. International Journal of Applied Earth Observation and Geoinformation 27: 53-62.

36. Le Mauff B, Juigner M, Ba A, Robin M, Launeau P, Fattal P. 2018. Coastal monitoring solutions of the geomorphological response of beach-dune systems using multi-temporal LiDAR datasets (Vendée coast, France). Geomorphology 304: 121-140.

37. Li S. et al, 2010. Wind-driven Land Degradation and its Control in Xizang, Tibet, in Chinese. Science Press, Beijing.

38. Li Y, Yu HY, Wang Y, Wu JP, Yang L. 2019. Classification of urban vegetation based on unmanned aerial vehicle reconstruction point cloud and image. Remote sensing for land and resources 31(01): 149-155. (in Chinese with English Abstract)

39. Liao YJ, Hu Y, Ye T. 2018. Construct 3D model based on low-altitude UAV oblique photography. Beijing Surveying and Mapping 32(05): 504-507. (in Chinese with English Abstract)

40. Martínez-Carricondo P, Agüera-Vega F, Carvajal-Ramírez F, Mesas-Carrascosa FJ, García-Ferrer A,

Pérez-Porras FJ. 2018. Assessment of UAV-photogrammetric mapping accuracy based on variation of ground control points. International journal of applied earth observation and geoinformation 72: 1-10.

41. Nield JM, Wiggs GF. Squirrell RS. 2011. Aeolian sand strip mobility and protodune development on a drying beach: examining surface moisture and surface roughness patterns measured by terrestrial laser scanning. Earth Surface Processes and Landforms 36(4): 513-522.

42. Qiang MR, Jin YX, Liu XX, Song L, LiH, Li FS, Chen FH, 2016. Late Pleistocene and Holocene aeolian sedimentation in Gonghe Basin, northeastern Qinghai-Tibetan Plateau: Variability, processes, and climatic implications. *Quaternary Science Reviews* 132: 57-73.

43. Qian GQ, Yang ZL, Dong ZB, Tian M. 2019. Three-dimensional morphological characteristics of barchans dunes based on photogrammetry with UAV. Journal of desert research 39(01): 18-25. (in Chinese with English Abstract)

44. Scarelli FM, Cantelli L, Barboza EG, Rosa MLC, Gabbianelli G. 2016. Natural and Anthropogenic coastal system comparison using DSM from a low cost UAV survey (Capão Novo, RS/Brazil). Journal of Coastal Research 75(sp1): 1232-1237.

45. Scarelli FM, Sistilli, F, Fabbri S, Cantelli L, Barboza EG, Rosa MLCC, Gabbianelli G. 2017. Seasonal dune and beach monitoring using photogrammetry from UAV surveys to apply in the ICZM on the Ravenna coast (Emilia-Romagna, Italy). Remote Sensing Applications: Society and Environment 7: 27-39.

46. Sauerbier M, Eisenbeiss H. 2010. UAVs for the documentation of archaeological excavations. International Archives of Photogrammetry. Remote Sensing and Spatial Information Sciences 38(Part 5): 526-531.

47. Seymour AC, Ridge JT, Rodriguez, AB, Newton E, Dale J, Johnston DW. (2018). Deploying Fixed Wing Unoccupied Aerial Systems (UAS) for Coastal Morphology Assessment and Management. Journal of Coastal Research, 34(3):704-717.

48. Sofia G, Hillier JK, Conway SJ. 2016. Frontiers in geomorphometry and earth surface dynamics: possibilities, limitations and perspectives. Earth Surface Dynamics 4(3): 721-725.

49. Solazzo D, Sankey JB, Sankey TT. Munson SM. 2018. Mapping and measuring aeolian sand dunes with photogrammetry and LiDAR from unmanned aerial vehicles (UAV) and multispectral satellite imagery on the Paria Plateau, AZ, USA. Geomorphology 319: 174-185.

50. Taddia Y, Corbau C, Zambello E, Pellegrinelli A. 2019. UAVs for structure-from-motion coastal monitoring: a case study to assess the evolution of embryo dunes over a two-year time frame in the Po River Delta, Italy. Sensors 19(7): 1717.

51. Tarolli P. 2014. High-resolution topography for understanding Earth surface processes: Opportunities and challenges. Geomorphology, 216, pp.295-312.

52. Valkaniotis S, Papathanassiou G, Ganas A. 2018. Mapping an earthquake-induced landslide based on UAV imagery; case study of the 2015 Okeanos landslide, Lefkada, Greece. Engineering Geology 245: 141-152.

53. Young EJ. 2012. Section 2.1.3: dGPS. In: Clarke LE, Nield JM. (Eds.) Geomorphological Techniques (Online Edition). British Society for Geomorphology:London, UK.

54. Yang JQ. 2018. Research on reconstruction method of building 3D model based on unmanned aerial vehicle images. Urban Roads Bridges and Flood Control, (11): 189-193. (in Chinese with English Abstract)

55. Zhang EY, Gao SS. 2018. Large-scale urban topographic map updating and revising based on UAV oblique photogrammetry. Standardization of Surveying and Mapping 34(04): 59-62. (in Chinese with English Abstract)

56. Zhang P. 2018. The application research on fusion of oblique photography and laser scanning technology in 3D city modeling. Urban Geotechnical Investigation and Surveying (04): 99-103. (in Chinese with English Abstract)

Table 1. Location error of UAV 3D modeling with different flight heights. The position error of GCPs (E_{GCPs}) and CPs (E_{CPs}) measured by horizontal RMSE ($RMSE_H$) and vertical RMSE ($RMSE_V$) at different flights are given together with the number of GCPs (N_{GCPs}) and CPs (N_{CPs}).

Site	Height/ m	N_{GCPs}*	N_{CP}	E_{GCPs}/m		E_{CPs}/m	
				$RMSE_H$	$RMSE_V$	$RMSE_H$	$RMSE_V$
D	74	26	4	0.049	0.043	0.055	0.053
D	90	20	4	0.044	0.027	0.078	0.04
D	110	25	4	0.046	0.028	0.057	0.023
D1	40	5	5	0.013	0.003	0.076	0.042
D1	50	5	5	0.072	0.046	0.074	0.042
B1	40	25	11	0.019	0.017	0.026	0.031
B1	50	25	11	0.020	0.052	0.028	0.024
B1	74	25	11	0.020	0.016	0.029	0.023
B2	60	22	6	0.065	0.016	0.076	0.032
B2	80	24	6	0.018	0.019	0.024	0.050

Note that: (*) some GCPs were destroyed or buried due to a strong wind event during the experiment in field.

Table 2. Location error of UAVs 3D modeling with different overlap degrees. The position error of GCPs (E_{GCPs}) and CPs (E_{CPs}) measured by horizontal RMSE ($RMSE_H$) and vertical RMSE ($RMSE_V$) at different overlaps are given together with the number of GCPs (N_{GCPs}) and CPs (N_{CPs}).

Site	Overlap (Heading / Sideways) /%	N_{GCPs}*	N_{CPs}	E_{GCPs}/m		E_{CPs}/m	
				$RMSE_H$	$RMSE_V$	$RMSE_H$	$RMSE_V$
D	85/70	26	4	0.049	0.043	0.055	0.053
D	70/65	25	4	0.044	0.024	0.090	0.046
D	65/60	27	4	0.042	0.011	0.073	0.055
B1	85/70	25	10	0.019	0.017	0.026	0.031
B1	75/55	24	10	0.012	0.005	0.032	0.036

Note that: (*) some GCPs were destroyed or buried due to a strong wind event during the field experiment.

Table 3. Position error of UAVs 3D modeling with different camera tilt angles. The position error of GCPs (E_{GCPs}) and CPs (E_{CPs}) measured by horizontal RMSE ($RMSE_H$) and vertical RMSE ($RMSE_V$) at different camera tilt angles are given together with the number of course (N_{course}), the number of GCPs (N_{GCPs}) and CPs (N_{CPs}).

Site	Camera tilt angle/Height	N_{Course}	N_{GCPs}	N_{CPs}	E_{GCPs}/m		E_{CPs}/m	
					$RMSE_H$	$RMSE_V$	$RMSE_H$	$RMSE_V$
D	-90°/74 m	1	26*	7	0.049	0.043	0.055	0.053
D	-45°/74 m	3	23*	7	0.045	0.034	0.052	0.100
D	-20°/74 m	3	21*	7	0.053	0.044	0.143	0.270
B1	-90°/74 m	1	24**	10	0.020	0.023	0.028	0.024
B1	-45°/74 m	3	24**	10	0.022	0.021	0.027	0.022
B1	-90°/40 m	1	16**	10	0.018	0.019	0.030	0.038
B1	-60°/40 m	3	16**	10	0.027	0.021	0.030	0.043

Note that: (*) some GCPs were buried due to a strong wind event during the experiment in dune field. (**) the number of GCPs were different due to the surveyed area at 74 m was different from that at 90 m in Site B1.

Table 4. Location error of UAV 3D modeling with different density of ground control points ($D_{GCPs,}$ calculated by number of ground control points divided by the flight area). The position error of GCPs (E_{GCPs}) and CPs (E_{CPs}) measured by horizontal RMSE ($RMSE_H$) and vertical RMSE ($RMSE_V$) at different number of GCPs are given together with the number of CPs (N_{CPs}).

Site	D_{GCPs} /km^2	N_{GCPs}	N_{CPs}	E_{GCPs}/m		E_{CPs}/m	
				$RMSE_H$	$RMSE_V$	$RMSE_H$	$RMSE_V$
D	38	34	7	0.017	0.026	0.023	0.071
D	29	26	7	0.016	0.018	0.028	0.069
D	17	15	7	0.011	0.024	0.038	0.093
D	11	10	7	0.014	0.035	0.040	0.117
D	6	5	7	0.005	0.003	0.041	0.274
D	0	0	7	/	/	0.691	26.973
B1	116	33	21	0.015	0.021	0.037	0.052
B1	84	24	21	0.013	0.024	0.038	0.051
B1	67	19	21	0.014	0.057	0.036	0.059
B1	42	12	21	0.010	0.043	0.039	0.055
B1	25	7	21	0.009	0.051	0.042	0.093
B1	0	0	21	/	/	0.673	0.106

Table 5. Position error of UAVs 3D modeling with different distribution of control points. The position error of GCPs (E_{GCPs}) and CPs (E_{CPs}) measured by horizontal RMSE ($RMSE_H$) and vertical RMSE ($RMSE_V$) at different GCPs' distribution mode are given together with the number of GCPs (N_{GCPs}) and CPs (N_{CPs}).

Site	Distribution mode	N_{GCPs}	N_{CPs}	E_{GCPs}/m		E_{CPs}/m	
				$RMSE_H$	$RMSE_V$	$RMSE_H$	$RMSE_V$
D	uneven	15	7	0.017	0.027	0.087	0.363
	even	15	7	0.010	0.024	0.038	0.093
B1	uneven	19	21	0.012	0.027	0.036	0.060
	even	19	21	0.014	0.057	0.032	0.046

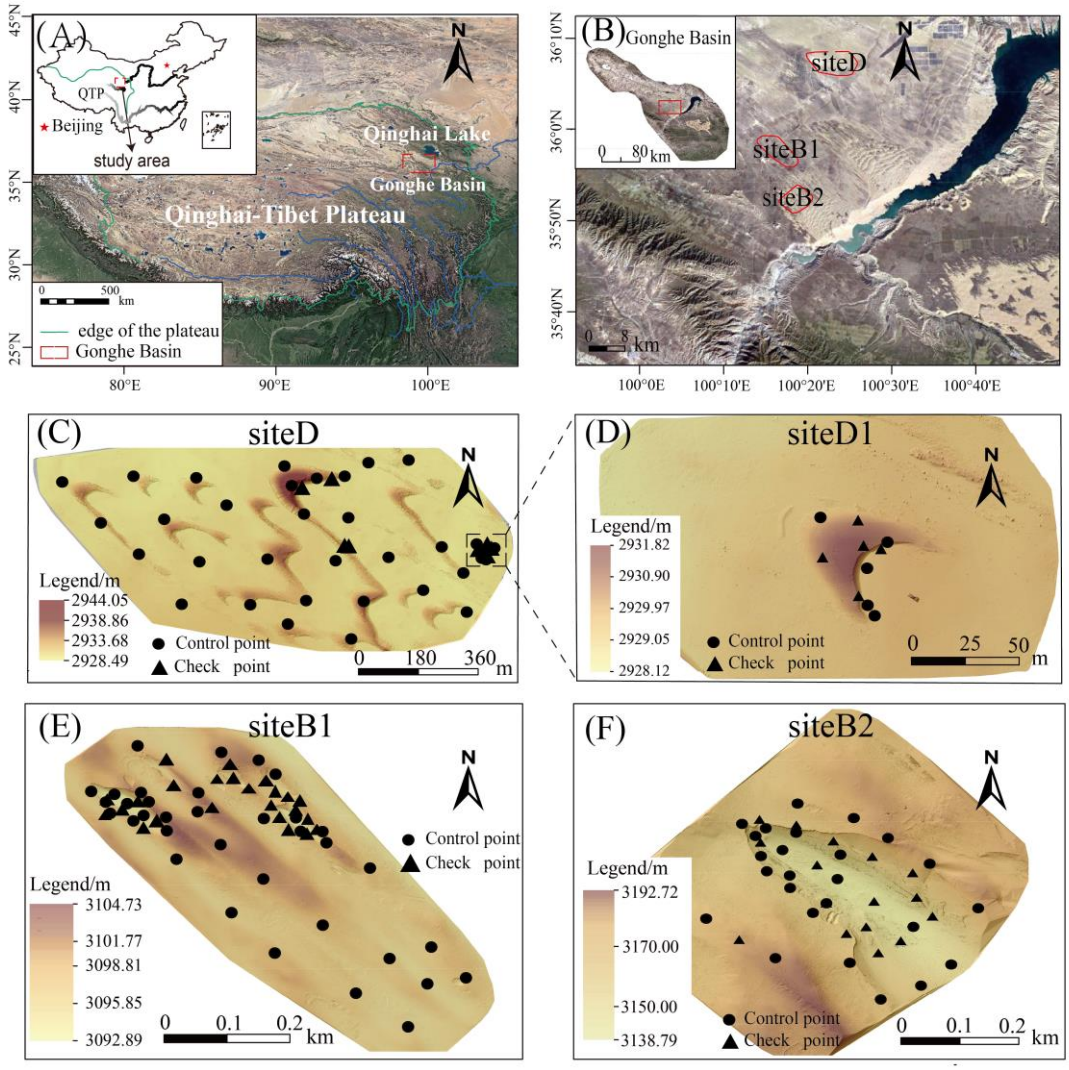

Figure 1. Landscape and the location of the study area. (A) Landscape map of the Qinghai-Tibet Plateau (QTP) and the study area. (B) Locations of the three study sites in the Gonghe Basin. (C)、(D)、(E)、(F) showed the GCPs (Ground Control Points, using for the coordinate system calibration) and the CPs (Check Points, used for checking the accuracy of the 3D reconstruction model) on the orthophotos at each study site.

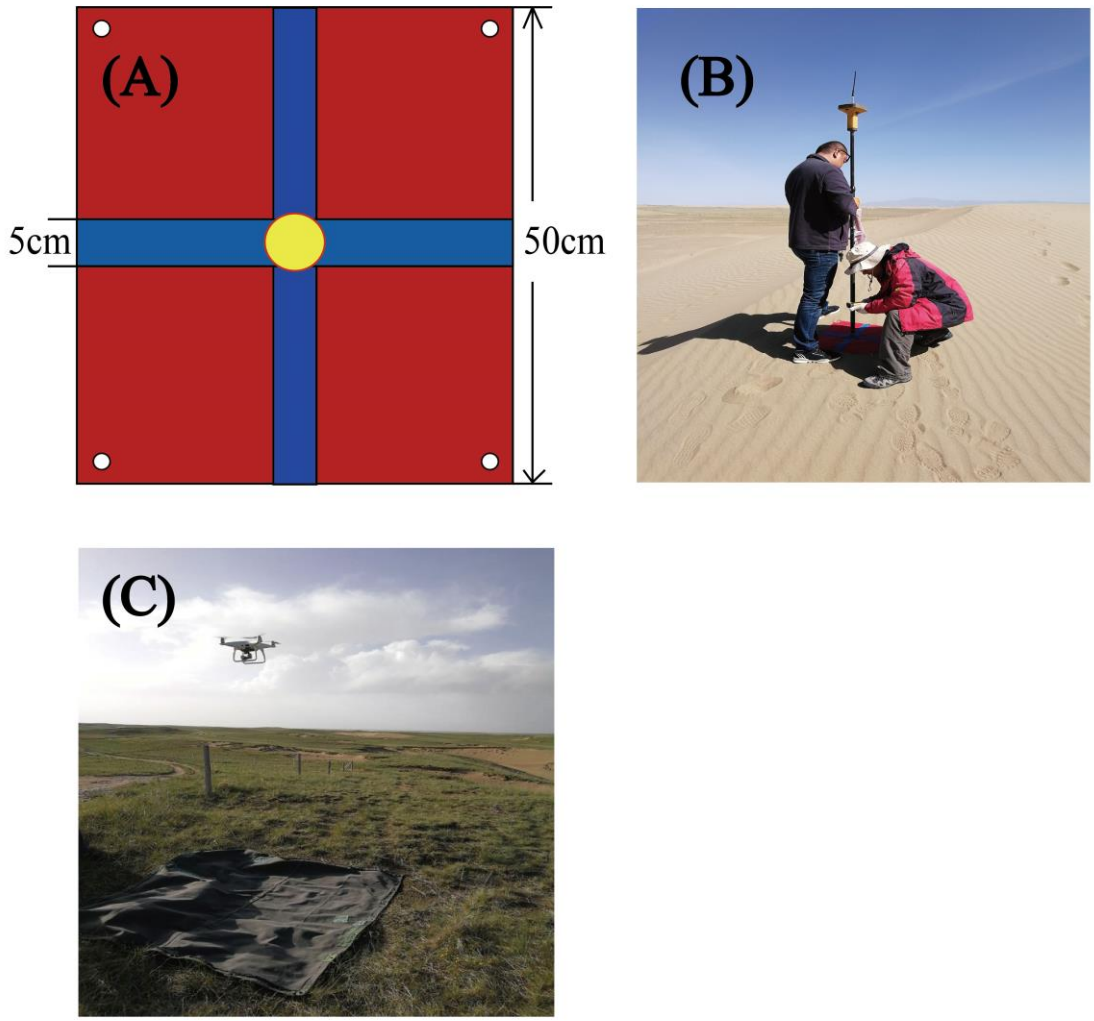

Figure 2. Pictures of the field UAV flying and measurement of the GCPs. (A) The customized GCPs sign is made of cloth material. The middle hole was used for the wooden stake to pass through, and the four corner holes were used to fix the sign. (B) The coordinate measurement of the GCPs. (C) Picture of the UAV performing a flight mission.

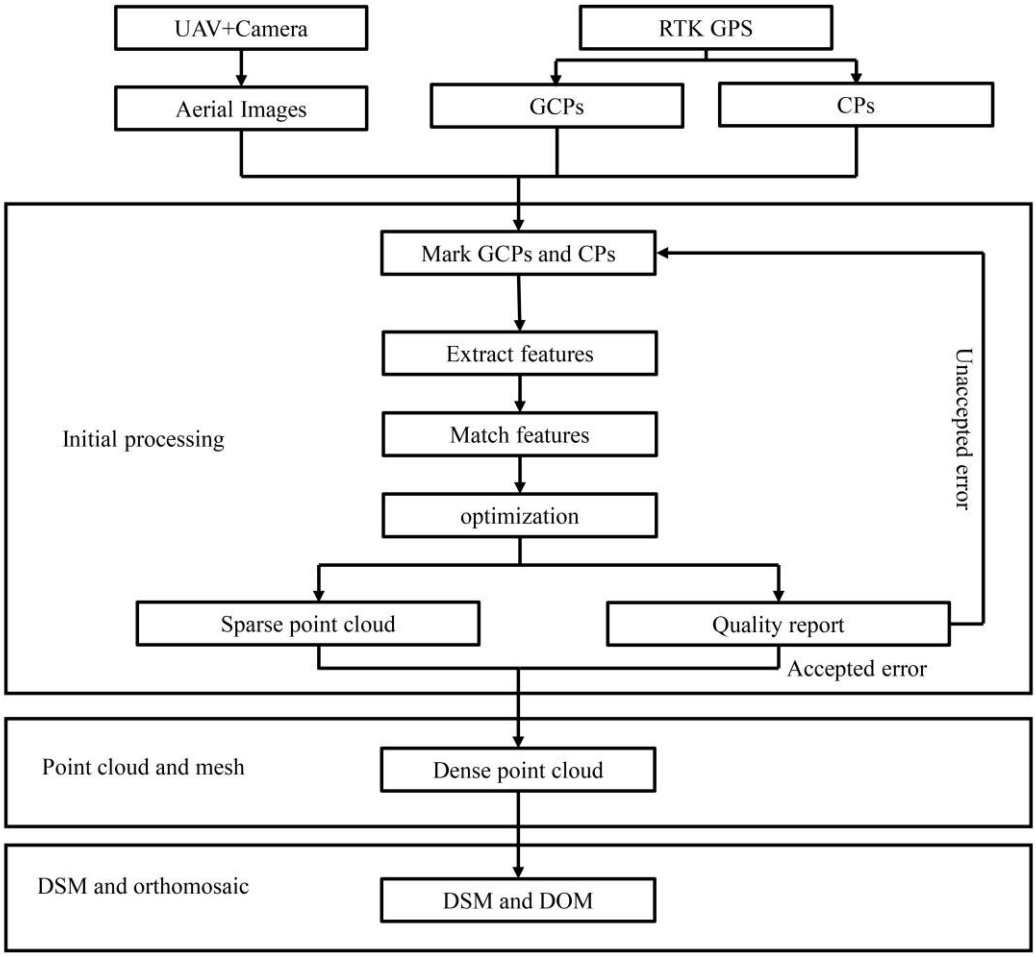

Figure3. Photogrammetric workflow of the UAVs in PIX 4D mapper software.

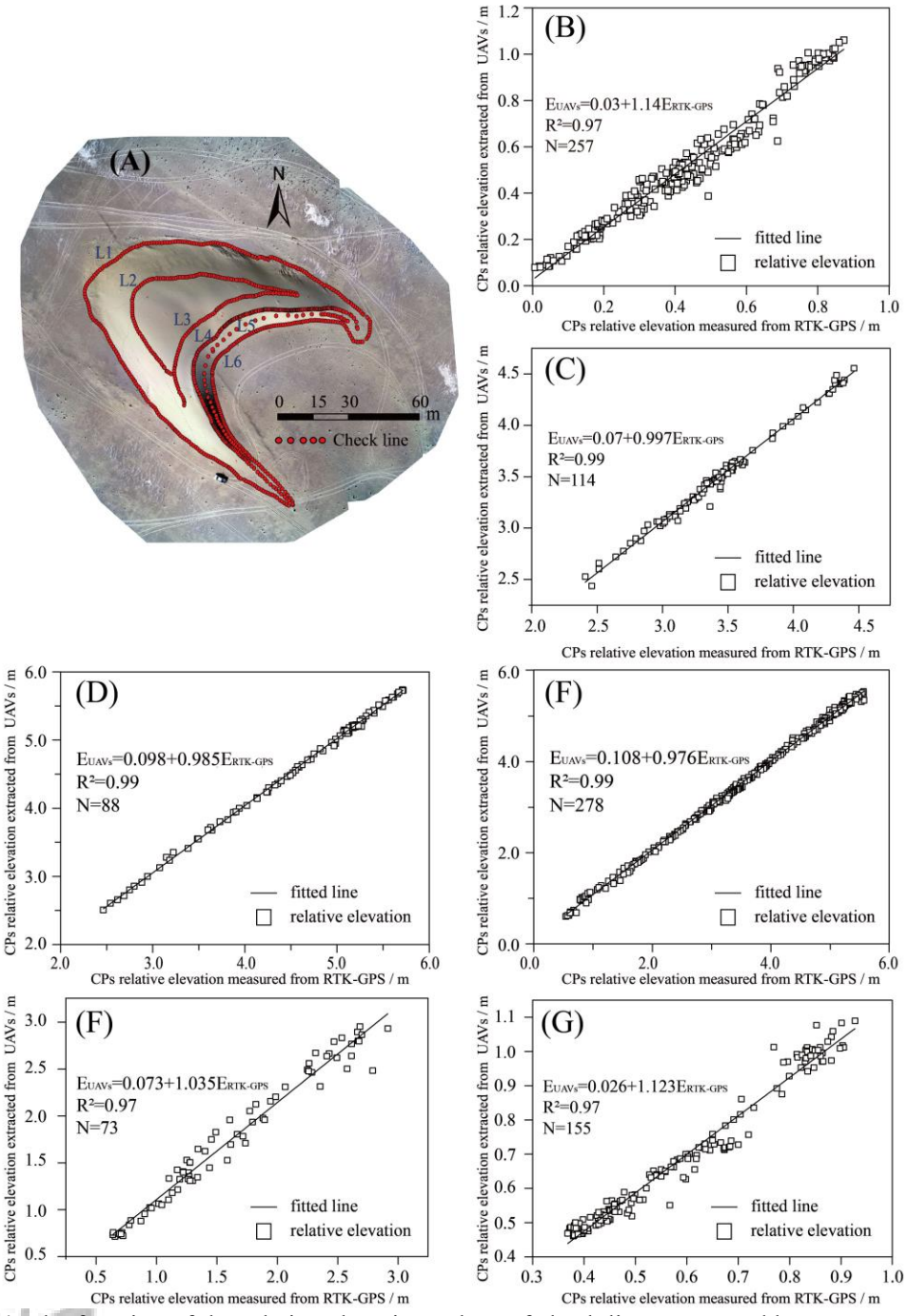

Figure 4. The function of the relative elevation values of check lines measured by RTK-GPS and extracted from the UAVs reconstructed 3D model on different parts of the targeted dune at site D. (A): check lines and their location on the different parts of the dune, (B): the function of L1 at the stoss slope base, (C): the function of L2 at 1/4 stoss slope, (D): the function of L3 at 3/4 stoss slope of the dune, (E): the function of L4 at the dune ridge,(F): the function of L5 at 1/2 lee slope, (G): the function of L6 at the lee slope base, N was the number of points per check line for fitting analysis. E_{UAVs} represents the relative elevation of CPs derived from UAVs reconstructed model, $E_{RTK\text{-}GPS}$ represents the same point relative elevation measured by RTK-GPS in field. The relative elevation of check lines was calculated through minus a basal value (2929 meters, the lowest elevation of the CPs of the dune).

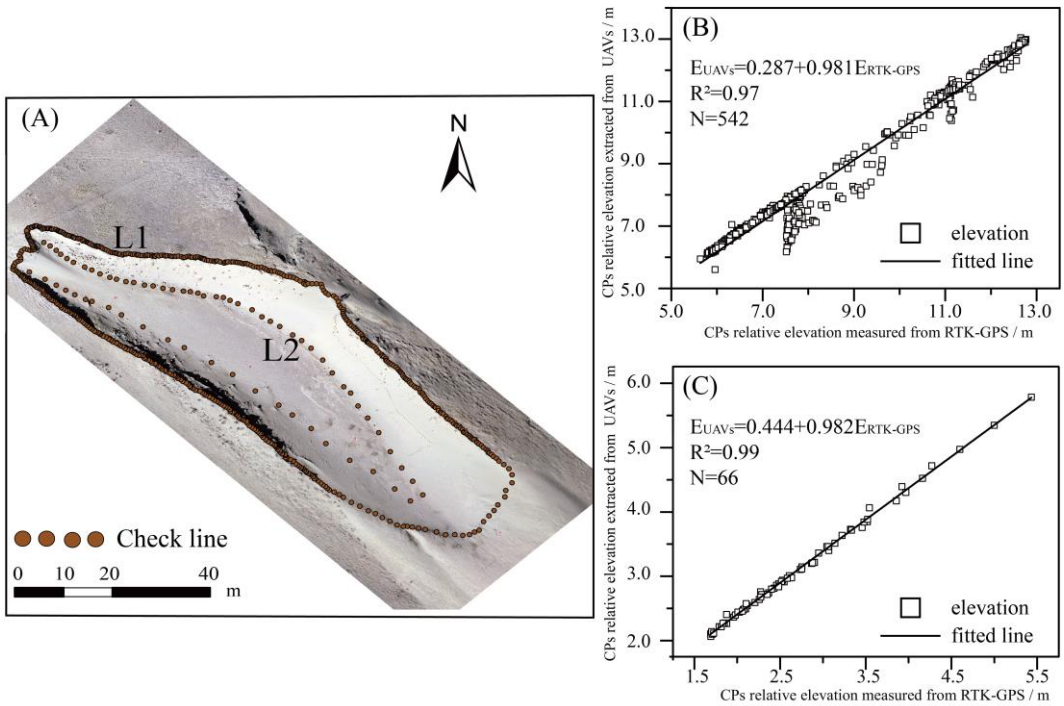

Figure 5. The function of the relative elevation values of check lines measured by RTK-GPS and extracted from the UAVs reconstructed 3D model on different parts of targeted blowout at site B1. (A): check lines and their location on the different parts of the blowout, (B): the function of L1 at the margin on the blowout, (C): the function of L2 at 1/2 on the slope of the blowout, N was the number of points in per check line for fitting analysis. E_{UAVs} represents the relative elevation of CPs derived from UAVs reconstructed model, $E_{RTK-GPS}$ represents the same point relative elevation measured by RTK-GPS in field. The relative elevation of check lines was calculated through minus a basal value (3090 meters, the lowest elevation of the CPs of the blowout).

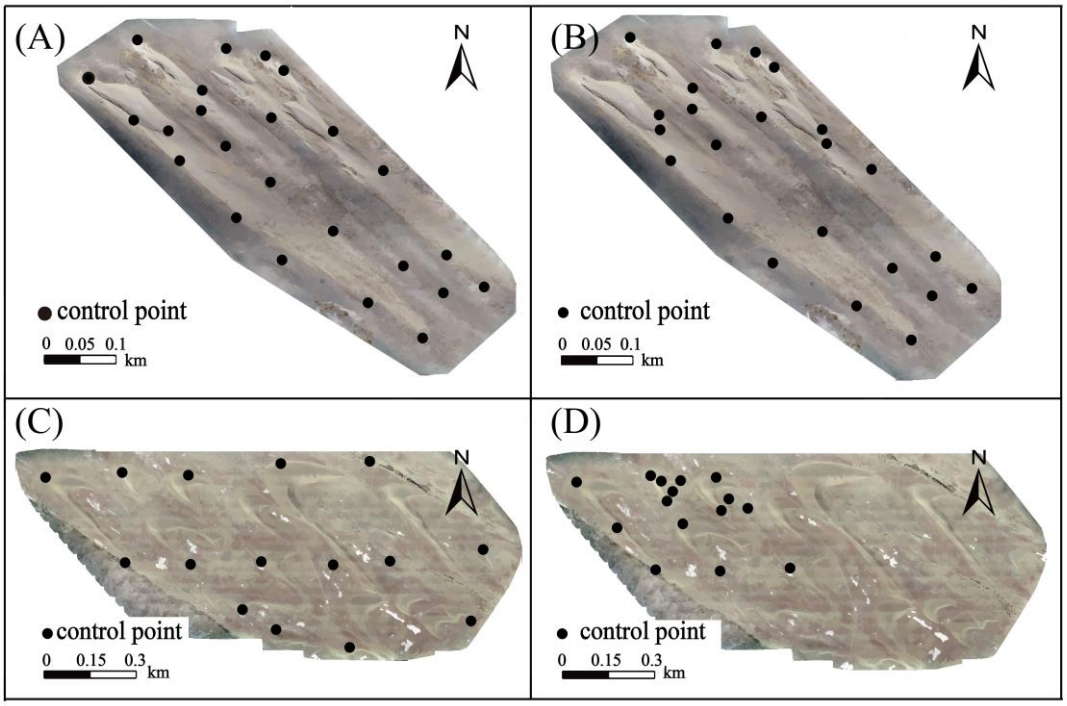

Figure 6. Schematic diagram of the distribution of GCPs. (A): Evenly distributed GCPs at site B1. (B): Unevenly distributed GCPs at site B1. (C): Evenly distributed GCPs at site D. (D): Unevenly distributed GCPs at site D.

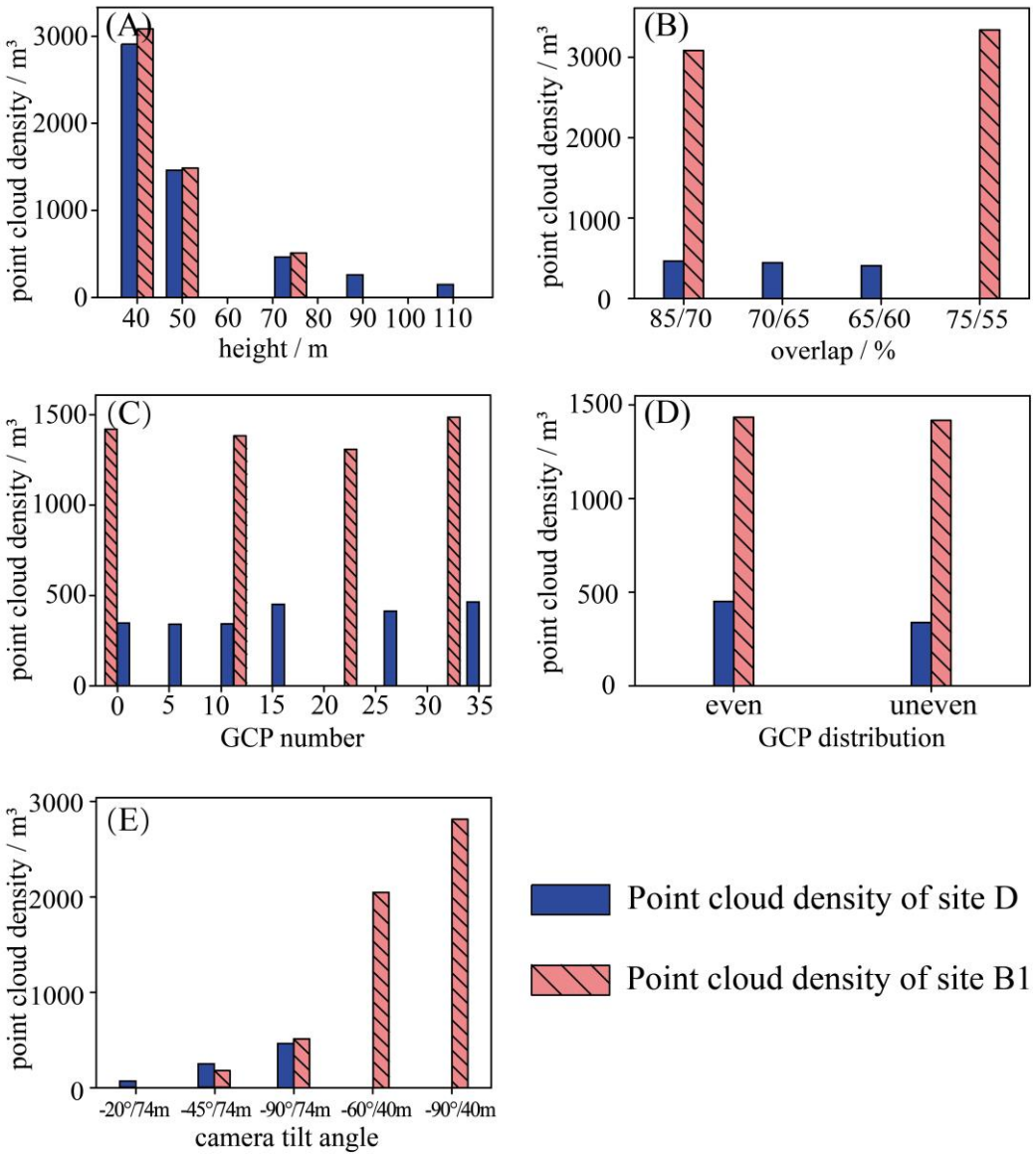

Figure 7. Point clouds density variation with different flight parameters. (A)-(E) respectively represented the point cloud density under different flight latitudes, different photo overlaps, different GCPs numbers, different distribution of the GCPs and different camera tilt angles.

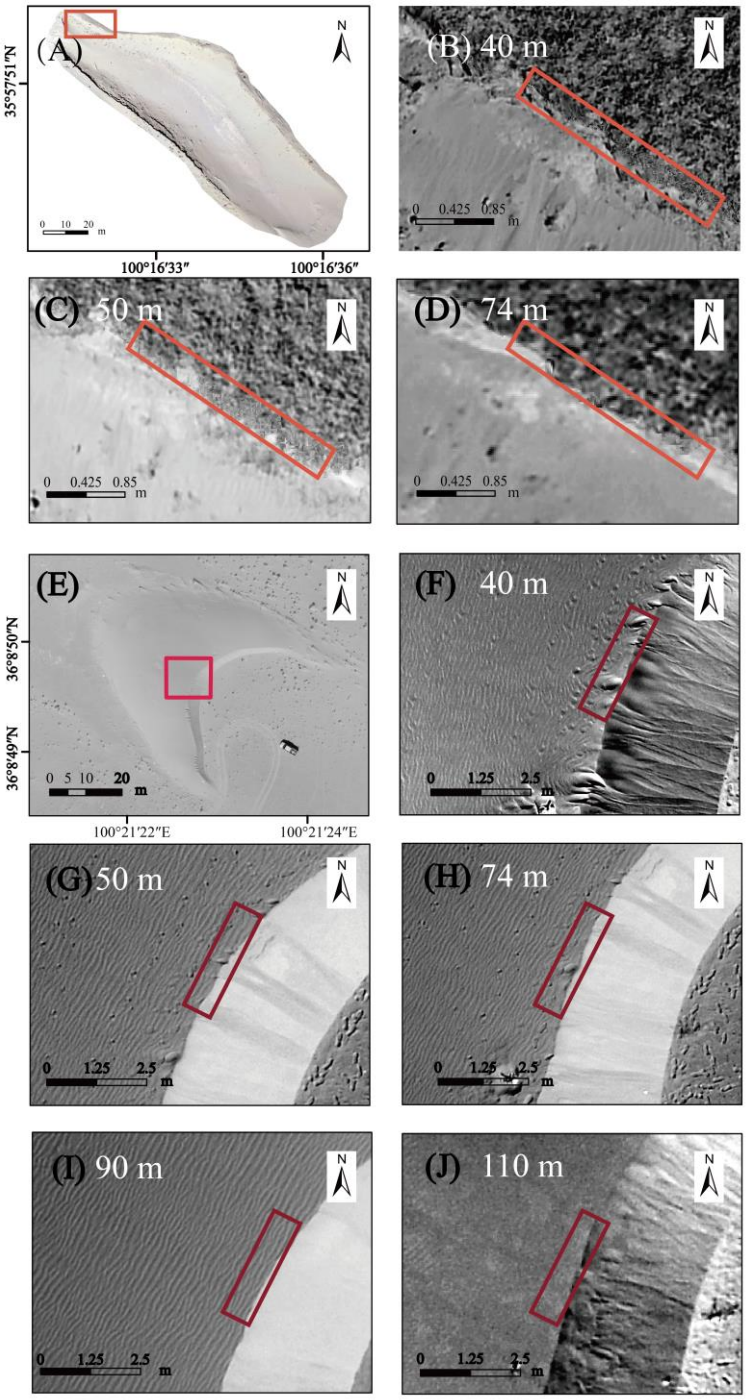

Figure 8. Comparison about the orthoimage's texture effect between different flight heights. (A) The whole orthoimage of site B1 at the height of 50 m. Orthophotos (B)、(C)、(D) respectively represented the partial texture effect of site B1 at different heights. (E)The whole orthoimage of site D1. Orthophotos (F)-(J) respectively represented the partial texture effect of site D1 at different heights.

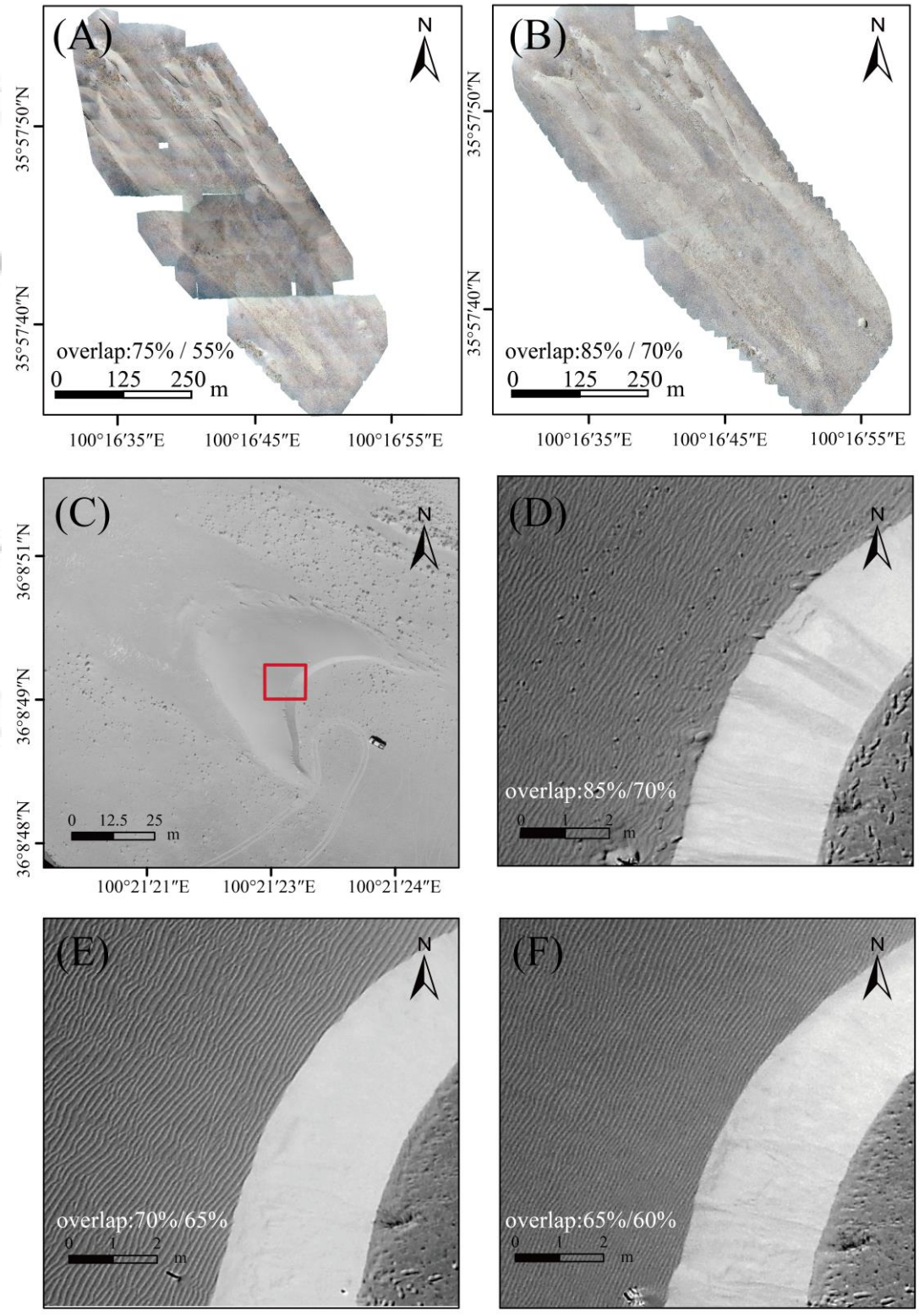

Figure 9. Comparison about the orthoimage's texture effect among different photo overlaps. Orthophotos (A) and (B) respectively represented the whole DOM of site B1 of different overlap. Orthophoto C was the whole DOM of site D1. Orthophoto (D)、(E)、(F) respectively represented the partial texture effect of site D1 at different overlap.

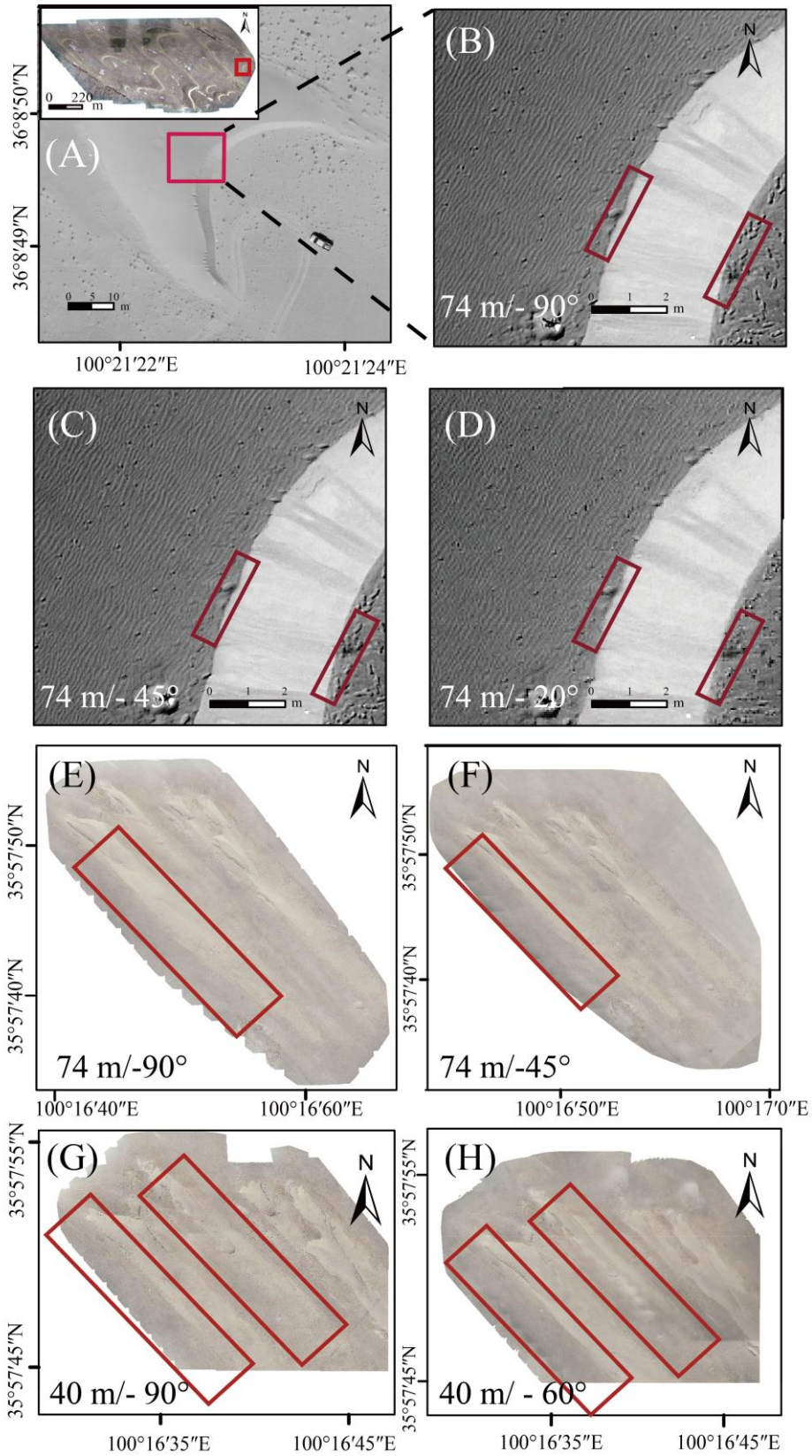

Figure 10. Comparison of the orthoimage's texture effect using different camera angles. (Orthophoto (A) was the whole orthoimage of site D1. (B)-(D) are DOMs of site D of different overlap, (E)-(H) are DOMs of site B1 of different overlap.)

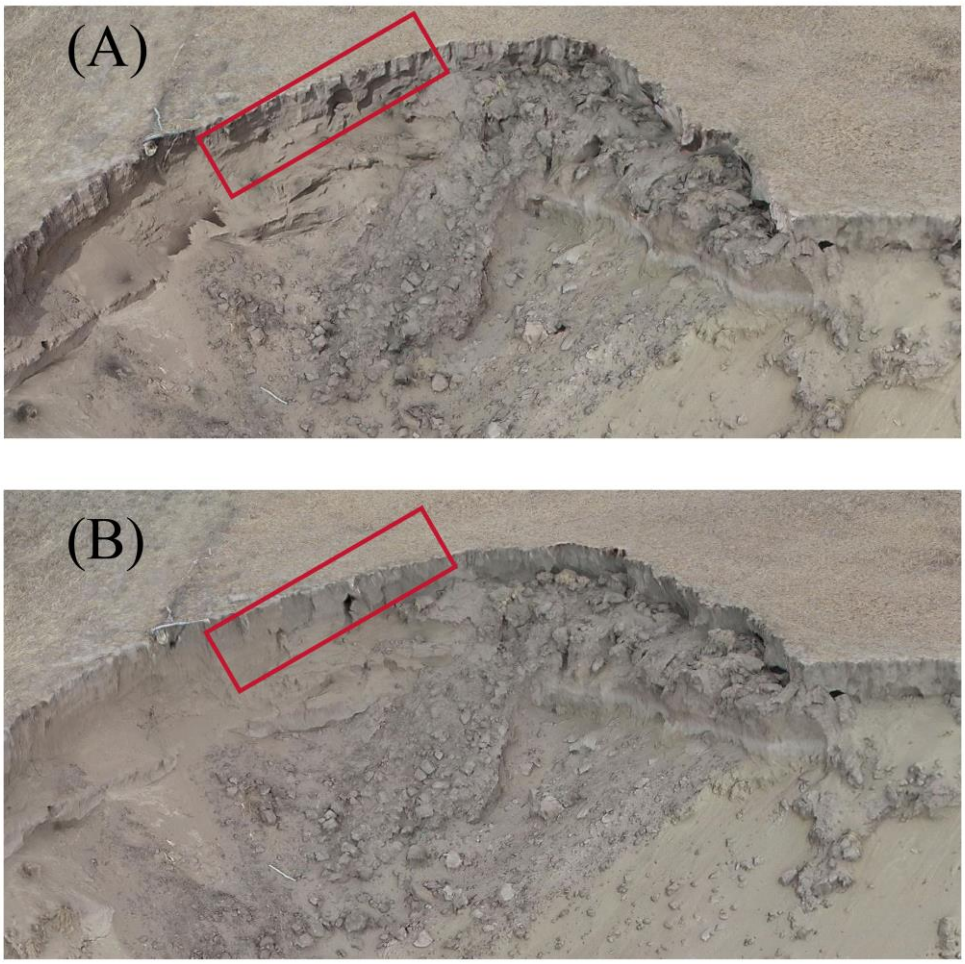

Figure 11. Comparison of 3D effects between vertical and tilt photography model of site B2 (100° 17′ 17″ E, 35° 53′ 49″ N). (A) Tilt photography. (B) Vertical photography.

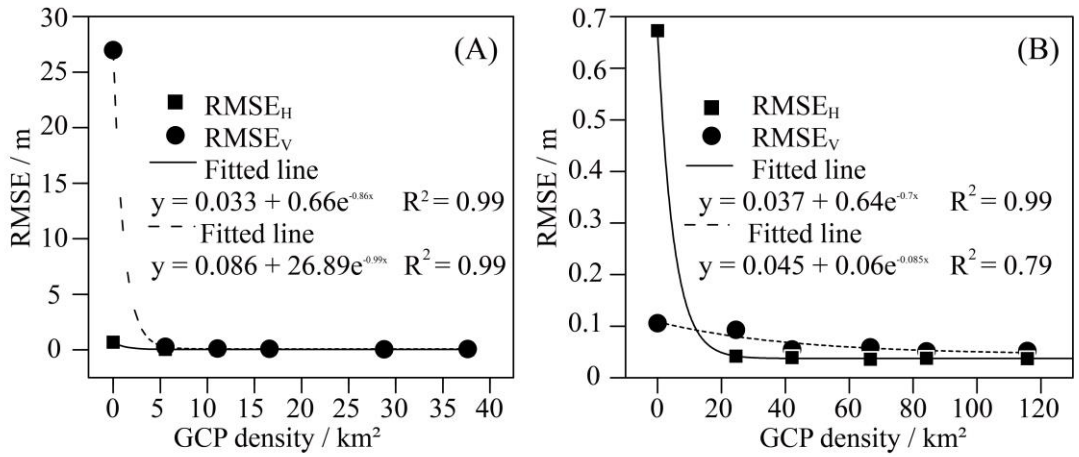

Figure 12. The function of the GCPs' density and the accuracy of 3D modelling. (A showed the function between the GCPs' density and the horizontal and vertical error of the 3D modeling at site D. B showed the function between the GCPs' density and the horizontal and vertical error of the 3D modeling at site B1.)

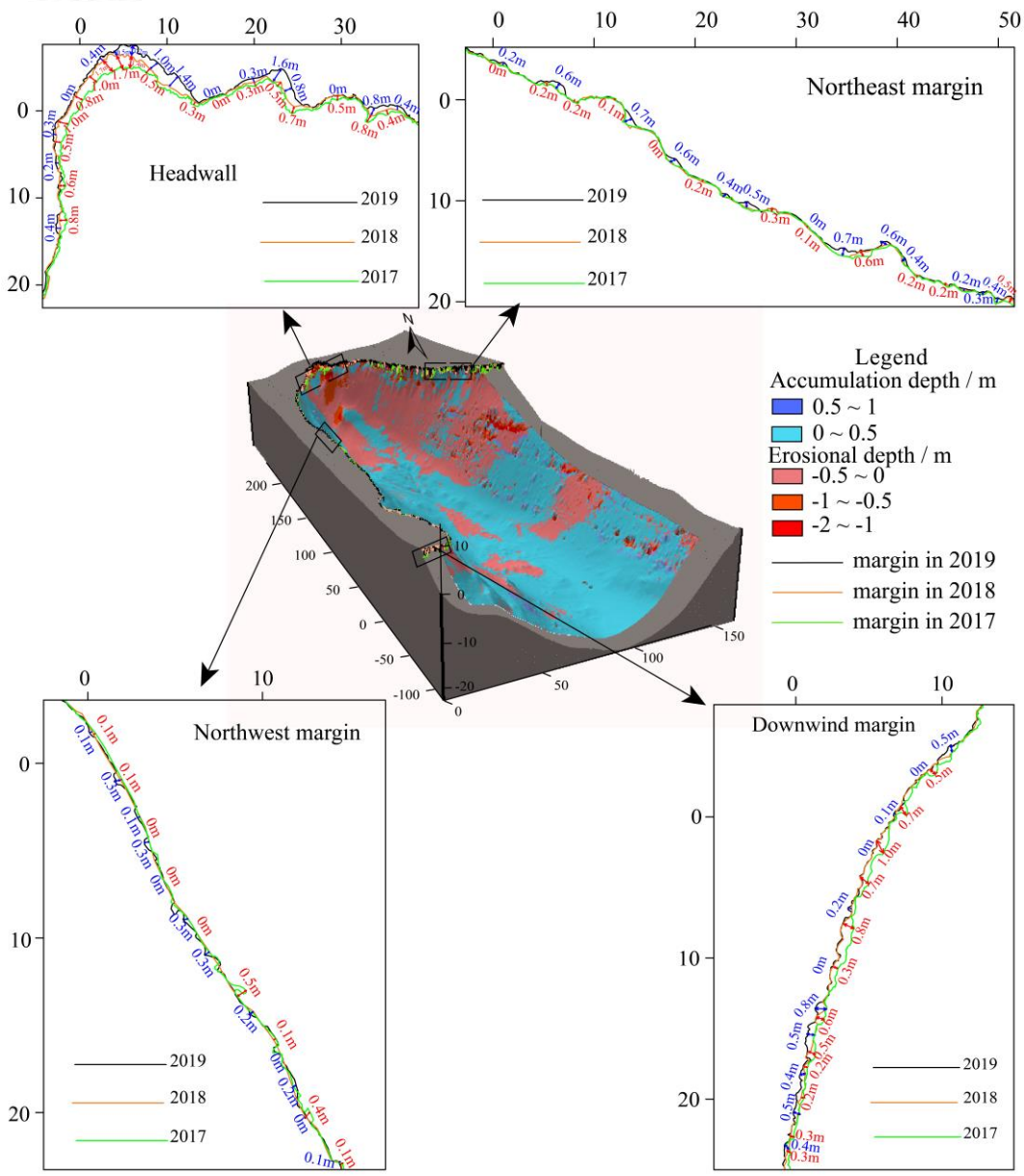

Figure 13. Topographical expansion or change between the 2017 and 2019 UAV surveys of the blowout at site B2. The middle model shows the depositional and erosional depths of different parts of the blowout from 2017 to 2019. The other four pictures show the annual changes of each part of the blowout margin.

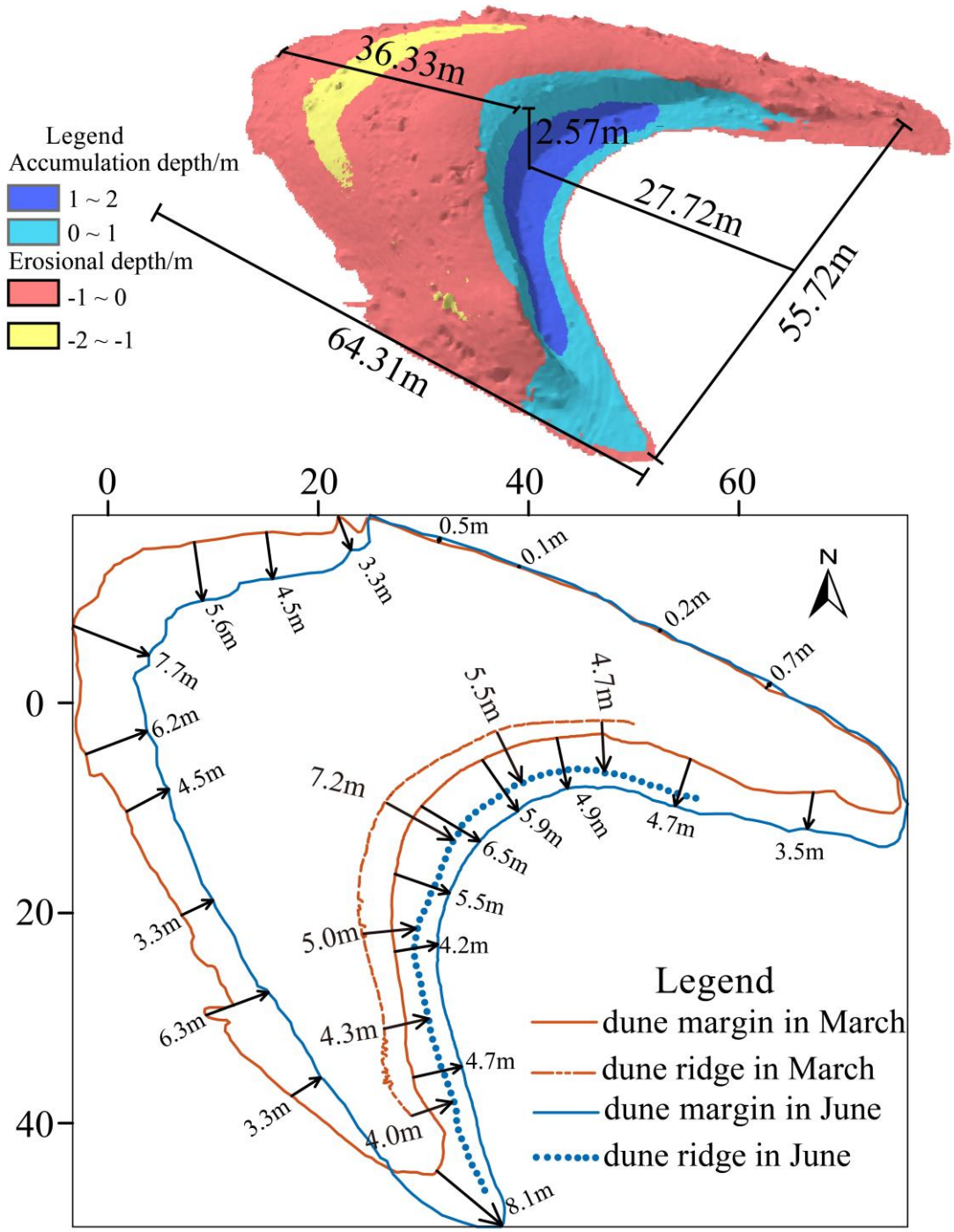

Figure 14. Topographical changes between the March and June UAV surveys in 2019 of the barchan dune at site D1. The model shows the parameters of dune morphology, and also indicates the sand accumulation and erosional depths of different parts of the dune from March to June in 2019. The lower plot shows the changes of each part of the dune margin and dune ridge.